# DESIGN AND MODELING OF A RESONANT INDUCTIVELY COUPLED WIRELESS POWER TRANSFER SYSTEM FOR MICRO AERIAL VEHICLES

by

Gregory Michael Plaizier

A thesis submitted to the faculty of
The University of Utah
in partial fulfillment of the requirements for the degree of

Master of Science

Department of Mechanical Engineering

The University of Utah

May 2018

**The University of Utah Graduate School**

# STATEMENT OF THESIS APPROVAL

The thesis of **Gregory Michael Plaizier**

has been approved by the following supervisory committee members:

| | | |
|---|---|---|
| **Shadrach J. Roundy** | , Chair | **01/24/2018** Date Approved |
| **Kam K. Leang** | , Member | **01/05/2018** Date Approved |
| **Darrin J. Young** | , Member | **01/05/2018** Date Approved |

and by **Tim Ameel**, Chair of

the Department of **Mechanical Engineering**

and by David B. Kieda, Dean of The Graduate School.

# ABSTRACT

This thesis discusses the design, modeling, and experimental validation of an inductively coupled wireless power transfer (WPT) system to power a micro aerial vehicle (MAV) without an onboard power source. MAVs are limited in utility by flight times ranging from 5 to 30 minutes. Using WPT for MAVs, in general, extends flight time and can eliminate the need for batteries. In this paper, a resonant inductive power transfer system (RIPT), consisting of a transmit ($T_x$) coil on a fixed surface and a receive ($R_x$) coil attached to the MAV, is presented, and a circuit is described. The RIPT system design is modeled to determine a suitable geometry for the coils, and the model validated experimentally. It is found that for the MAV used in this work, a suitable geometry of coils is a 19cm diameter planar spiral $T_x$ coil made with 14 AWG copper wire, seven turns, and 5cm pitch paired with an $R_x$ coil made of 16-20AWG wire, 13cm–20cm diameter, 1mm pitch, and one to two turns. A demonstration of an MAV being powered 11cm above the $T_x$ coil with the WPT system in a laboratory setting is presented. The MAV consumes approximately 12 Watts. The overall power efficiency of the RIPT system from RF power source output to MAV motors is approximately 32%.

This thesis is dedicated to my wife, Emily, for her encouragement and support through the course of this work.

TABLE OF CONTENTS

ABSTRACT ..... iii

LIST OF TABLES ..... vii

LIST OF FIGURES ..... viii

LIST OF SYMBOLS AND ABBREVIATIONS ..... x

ACKNOWLEDGMENTS ..... xi

Chapters

1. INTRODUCTION ..... 1

    1.1 Motivation for this Project ..... 1
    1.2 Project Goals ..... 2

2. BACKGROUND OF WIRELESS POWER TRANSFER ..... 4

    2.1 Review of Different Forms of Wireless Power Transfer ..... 5
        2.1.1 Optic Wireless Power Transfer ..... 5
        2.1.2 Microwave Power Transfer ..... 5
        2.1.3 Capacitive Coupling ..... 6
        2.1.4 Inductive Coupling ..... 6
    2.2 Resonant Inductive WPT ..... 8
    2.3 Prior Work ..... 8

3. RESONANT INDUCTIVE COUPLING WIRELESS POWER TRANSFER ..... 11

    3.1 Circuit Theory on Resonant Inductive Coupling ..... 11
    3.2 Main Design Output Considerations for Resonant Inductive Coupling Theory 15
    3.3 Primary Parameter Considerations ..... 16
        3.3.1 Frequency ..... 16
        3.3.2 Coil Size and Geometry ..... 17
        3.3.3 Material Considerations ..... 19
        3.3.4 Two-Coil vs. Four-Coil WPT System ..... 20
        3.3.5 Impedance Matching ..... 21
    3.4 Planar Circular Spiral Coil Modeling ..... 24
        3.4.1 Inductance ..... 24
        3.4.2 Capacitance ..... 25

3.4.3 Resistance ..... 25

4. WIRELESS POWER TRANSFER SYSTEM VALIDATION ..... 27

4.1 Test Setup and Procedure ..... 27
4.2 System Characterization ..... 30

5. DESIGN OF RESONANT INDUCTIVELY COUPLED WPT SYSTEM FOR AN MAV ..... 34

5.1 Design Explanation ..... 34
5.2 Design Parameter Sensitivity Analysis ..... 35
5.3 Prototype Design ..... 46
5.3.1 Electronic Components ..... 55

6. FULL MAV SYSTEM VALIDATION ..... 58

6.1 Experimental Setup and Procedure ..... 58
6.2 Experimental Results ..... 60

7. FUTURE WORK AND CONCLUSION ..... 62

7.1 Future Work ..... 62
7.2 Conclusions ..... 63

REFERENCES ..... 65

LIST OF TABLES

Tables

4.1: Experimental values obtained for different $R_x$ coils and the 190mm outer diameter $T_x$ coil, with a coil separation of 100mm. ..... 30

4.2: Theoretical vs. experimental values are listed in this table for the $T_x$ coil. ..... 31

4.3: The theoretical and experimental values are shown in this table for the 13.7cm $R_x$ coil. The power values here are found using the $T_x$ coil as detailed above. ..... 32

4.4: Theoretical and experimental values are compared in this table for the 15.3cm $R_x$ coil. ..... 33

5.1: A table indicating the default parameters used in the sensitivity study..... 36

5.2: Summary of suitable $R_x$ coil parameters to provide an MAV with enough power to hover, achieving $\chi$ greater than 1. ..... 54

LIST OF FIGURES

Figures

1.1: A potential use for a wirelessly powered UAV in a hazardous environment. ..... 2

3.1: A two-port network is shown here ..... 13

3.2: A four-coil system consisting of (from left to right) a drive loop, $T_x$ oscillating coil, $R_x$ oscillating coil, and a load loop. ..... 21

4.1: A picture of a $T_x$ coil used in the experimental validation. ..... 28

4.2: A picture of two different $R_x$ coils is shown here. ..... 28

4.3: A picture displaying the test setup with (a) the WiBotic, Inc. power amplifier, (b) the SWR/Wattmeter, (c) the $T_x$ coil, (d) and the $R_x$ coil. ..... 29

4.4: The relationship between efficiency and axial misalignment using $R_x$ coil 1 and a 12.5Ω load is shown. ..... 31

5.1: Theoretical changes in $R_x$ ($d_{Rx}$) diameter affect χ with changing separation distances are shown. ..... 37

5.2: Changes in χ due to changing outer $R_x$ coil diameter and axial misalignment are shown. ..... 38

5.3: Frequency effects on χ due to changing misalignment. ..... 38

5.4: The effects of frequency on χ as coil separation changes are shown. ..... 39

5.5: A demonstration how changing the number of $R_x$ coil turns affects χ as axial alignment changes.. ..... 41

5.6: Changes to χ with different number of $R_x$ coil turns and changing separation. ..... 41

5.7: Differences in χ due to axial alignment changes using different wire diameters. ..... 42

5.8: The effects of wire diameter on χ with changing coil separation. ..... 43

5.9: Changes in $R_x$ pitch and misalignment as it affects χ. ..... 44

5.10: The effect of pitch on χ as separation changes. ..... 45

5.11: The relationship between thrust and power requirement of the UAV.....47

5.12: The effect on $\chi$ by the number of $R_x$ coil turns and outer diameter: (a) power required to lift the UAV, (b) efficiency of the WPT system, (c) $P_L$ and (d) $\chi$, according to the modeled equations. .....49

5.13: Performance of the WPT system when power input is limited by a maximum $V_{in}$ of 50V and maximum $I_1$ of 2A, which is approximately the limitations of the RF Power supply used in this work. .....50

5.14: The effect on $\chi$ by the number of $R_x$ coil turns and pitch: (a) power required to lift the UAV, (b) efficiency of the WPT system, (c) $P_L$ and (d) $\chi$, according to the modeled equations. .....51

5.15: An example of the effect on $\chi$ by the number of $R_x$ coil turns and pitch: (a) power required to lift the UAV, (b) efficiency of the WPT system, (c) $P_L$ and (d) $\chi$, according to the modeled equations. .....52

5.16: The effect on $\chi$ by the number of $R_x$ coil turns and wire diameter: (a) power required to lift the UAV, (b) efficiency of the WPT system, (c) $P_L$ and (d) $\chi$, according to the modeled equations.. .....53

5.17: The power input is limited to 100W, 50V, and 2A in this simulation. .....54

5.18: A simplified circuit model of the harmonic rectifier, adapted from [37], is shown here. .....56

5.19: The circuit model for the $R_x$ coil and power conditioning electronics is shown.....57

6.1: The WPT system with the MAV is shown here. The MAV is positioned on a platform approximately 90mm above the $T_x$ coil.. .....59

6.2: A display of the functioning MAV system being wirelessly powered.....60

# LIST OF SYMBOLS AND ABBREVIATIONS

| | |
|---|---|
| WPT | Wireless Power Transfer |
| RIPT | Resonant Inductive Power Transfer |
| MAV | Micro Aerial Vehicle |
| $T_x$ | Transmit side of the WPT system |
| $R_x$ | Receive side of the WPT system |
| $\chi$ | The figure of merit, defined as $P_L/P_{req}$ |
| $P_L$ | Power received at the load end of the WPT system |
| $P_{req}$ | The power required by the MAV to hover |
| $P_{in}$ | Power delivered into the WPT system from the RF power source |
| $Q$ | Quality factor |
| $k$ | Coupling coefficient between two inductively coupled coils |
| $k_c$ | Critical coupling coefficient between two coils |
| $M$ | Mutual inductance between two coils |
| $\eta$ | Efficiency of the WPT system, defined as $P_L/P_{in}$ |
| $\sigma$ | Conductivity |
| $\mu_0$ | Permeability of free space |
| $\delta$ | Skin depth of alternating current penetration to wire |

# ACKNOWLEDGMENTS

Thanks to Binh Truong for his help and added knowledge to aid in understanding and modeling of this project. Thanks to Bob Christensen for sharing his knowledge of WPT, without which this project would still be a work in progress. Also thanks to the senior design team who got this project underway: Erik Andersen, Derek Driggs, Taylor Howell, and Bryan Nay. I also want to thank Erik especially for working through problems with me over the course of the project.

I want to thank my committee members, Drs. Roundy, Leang, and Young, for their guidance throughout this project, and especially to Dr. Leang and Dr. Roundy for their constant help, guidance, correction, motivation, and instruction over the past several years.

# CHAPTER 1

# INTRODUCTION

Interest in unmanned aerial vehicles (UAVs) is growing in a variety of industries. In 2017 the sales of quadrotor UAVs is estimated to be nearly 30 times greater than sales in 2013 [1]. Recent technological advances have led to the development of high-performance UAVs, which include fixed-wing aircraft, flapping-wing aircraft, coaxial helicopters, trirotor helicopters, and the popular quadrotor helicopter. Quadrotor UAVs are used in many fields and are suited for use in a variety of applications, including detection of environmental hazards, search and rescue operations, and surveillance in areas dangerous for humans. Limited flight times impede utility of UAVs. Most small quad-rotor UAV flight times range from 5 to 20 minutes, with some approaching a 30-minute flight time. To increase the utility of UAVs, a more sustained flight is needed.

## 1.1 Motivation for this Project

Wireless power transfer (WPT) is a potential method to increase the flight time of micro aerial vehicles (MAVs) by providing an MAV with a constant source of power. This would eliminate the need for batteries, and provide a feasible alternative to exchanging batteries or landing an MAV to charge in a hostile environment, where doing so is impractical, as shown in Figure 1.1. A WPT system capable of providing enough power to an MAV to enable hovering would allow an MAV to charge in flight. The use

Figure 1.1: A potential use for a wirelessly powered MAV in a hazardous environment. A mobile ground robot might remain in close enough proximity to the MAV to allow it to return and charge [2].

of WPT for UAVs has been previously explored and several demonstrations have been performed in which a UAV was powered wirelessly via a laser [3], microwave transmission [4], and inductively coupled coils. This work provides understanding into the relationship between RIPT system design parameters and an MAV, so that the use of MAVs can be increased by decreasing MAV down time.

## 1.2 Project Goals

The goal of this project is to understand the design relationships of an inductive wireless power transfer system as it relates to a small (~20cm) MAV and build a working WPT system, which allows an MAV to hover near a transmit source with no onboard power source. The main consideration in the relationship between the MAV and the WPT system will be a figure of merit ($\chi$), which—for this work—is defined as the ratio of

power received at the load to power required by the MAV to hover, or

$$\chi = \frac{P_L}{P_{req}}, \tag{1.1}$$

where $P_L$ is the power received at the load and $P_{req}$ is the power required by the MAV to hover with a given coil payload.

The main contribution of this project is to model, analyze, design, and build an inductive WPT system, specifically for use with an MAV by analyzing how χ changes with altering WPT system parameters. Parameters such as number of coil turns, coil pitch, wire diameter, wire material, and frequency of operation are all factors to be considered. WPT system characteristics should also examine aspects, such as how the receive side will attach to the MAV and what affect misalignment or change in orientation will have on χ.

# CHAPTER 2

## BACKGROUND OF WIRELESS POWER TRANSFER

Wireless power transfer has been a fascination of scientists and engineers for over a century. The first recorded successful experiments with WPT occurred at the close of the 19th century when Nikola Tesla demonstrated WPT through inductive power transfer, capacitive power transfer, and resonant inductive power transfer. In 1903, he filed a patent from his discoveries enabling WPT [5]. The science and engineering communities lost interest in WPT after Tesla's experiments until the 1960s when William C. Brown used microwave technology for WPT based on technological advancements made during World War II [6]. The advancements made by Brown reignited interest in WPT via microwave transmission. In 1987, Canadian researchers powered an airplane using microwave power transfer [7]. Due to the size and safety concerns of microwave power transfer systems, commercialization of such systems is difficult. In 2006, interest for WPT via resonant inductive coupling increased after MIT researchers demonstrated WPT via non-radiative magnetic resonant coupling [8]. Since that time, many organizations and individuals have performed studies and experiments to expand the field of WPT via resonant inductive coupling. Products, such as wireless phone chargers and wireless toothbrush chargers, have been developed, as well as products such as wireless chargers for electric vehicles, which use inductive power transfer. Several other forms of WPT are in use and are discussed in this chapter.

## 2.1 Review of Different Forms of Wireless Power Transfer

Several different forms of WPT exist, including microwave, ultrasonic, capacitive coupling, inductive coupling, and light wave WPT. The benefits, issues, and basic operation of each of these mentioned are explored in more detail in the following sections.

### 2.1.1 Optic Wireless Power Transfer

Optic WPT, or light wave WPT, which uses lenses, lasers, and photocells, operates by using high powered lasers, which are directed at photocells to accomplish WPT. Photocells convert light spectrum and solar frequencies to electricity. Laser WPT is considered a far-field WPT technology because it can achieve great WPT distances, up to several kilometers. In 2012, a commercial engineering firm demonstrated laser WPT at least a kilometer away by powering a 17lb drone [9]. Using lasers for WPT requires the transmitting laser or focusing mirrors to have clear line of sight of the receiving photocells. Another issue is that high powered lasers must be carefully directed to ensure the safety of those around them. For use with MAVs, laser WPT systems are difficult to use because the photocell panels required on the receiving end can be large and heavy.

### 2.1.2 Microwave Power Transfer

Microwave WPT, as discussed earlier, was one of the earliest forms of WPT, which demonstrated significant advancements and utility. Microwave WPT is also a far-field WPT technology, which relies on radiative electromagnetic waves to accomplish the power transfer. Focused or omnidirectional RF transmitters emit radio waves or microwaves (generally in the GHz range) and rectennae receive the radiated microwaves

and convert it to DC power. Microwave power transmission has been considered for space applications because it can transmit over far distances. A major issue with using microwave power transmission commercially is safety for those in the beaming path. Microwave ovens use the same frequency and general mode of operation as transmitters used for power transmission, which can be unsafe if the power levels become large. For use with MAVs, the rectenna may be quite large to achieve sufficient power transfer.

### 2.1.3 Capacitive Coupling

Capacitive coupling, also known as electrostatic induction, is considered near-field WPT technology, and was patented in 1998 by A. Rozin [10]. This technique uses a high frequency signal to charge a capacitive plate and create a high frequency electric field. A secondary plate brought within a few centimeters creates a capacitive current, which can be rectified and used as DC current. The capacitive coupling technique results in high electric fields, which can quickly exceed safe limits. This technique also requires the secondary plate to remain close to the transmitting plate, which is impractical for applications with hovering MAVs. The resonant capacitive coupling technique operates under the same theory, but by tuning the plates to operate at the same frequency, separation distance can be increased to more than 10cm.

### 2.1.4 Inductive Coupling

Inductively coupled coils for WPT, as discussed above, were introduced first by Nikola Tesla [5]. Inductive power transfer relies on electromagnetic field and Maxwell's equations [10], and is considered a near-field technology. A primary coil is driven by a high frequency current, which creates an oscillating magnetic field. A secondary coil

captures the magnetic flux created by the primary coil and creates an oscillating current in the secondary coil, which can then be rectified and used as DC current. Loosely coupled coils are kept close together (a few centimeters) to achieve sufficient power transfer. Use of this technology can be found commercially today in wireless cellular phone chargers, wireless chargers for electric vehicles, and electric toothbrush chargers. Resonant inductive power transfer operates under the same theory, but the coils are tuned to resonate at the same frequency. This enables better coupling and greater distances between the coils, and can be considered mid-range power transfer.

Another variation of inductive power transfer is magnetic resonance coupling, which was first demonstrated by researchers at MIT [8]. The MIT researchers introduced a four-coil system: a driving single turn loop, a primary coil resonator, a secondary coil resonator, and a single turn load-side loop. By introducing the loops on either end of the resonator coils, the system has a higher quality factor when tuned correctly. The additional loops also provide an extra method of altering mismatched impedances between source and load of the system by decreasing or increasing the coupling coefficient between the loop and the coil on either side of the system. Several researchers have shown that the performance of either system is equivalent if the proper considerations are accounted for [11], [12].

For all types of inductive power transfer, the operation of such a system is safer than other methods of WPT for individuals nearby because the system relies on magnetic field rather than electric or radiative fields. One of the benefits of inductive power transfer is that a direct line of sight is not needed for efficient operation. When placed between coupled coils, conductive materials tend to decrease the efficiency of power transfer, but non-conductive materials have little effect.

## 2.2 Resonant Inductive WPT

For the purpose of wirelessly powering an MAV, the preferred method of WPT is resonant inductive power transfer (RIPT) due to its safe operation and its mid-range operating distance. The technique requires no moving parts for tracking, as optic or microwave power transfer do, so regular maintenance of motors or actuators is not required. Another desirable feature is that a line of sight is not needed, so it can be used through surfaces when an opening could be hazardous. RIPT has been investigated for use with dynamic loads, such as an MAV and proven to be successful [13]. The RIPT system also has a benefit that the coils can be designed such that impedance matching networks are not needed.

## 2.3 Prior Work

Since the first publication introducing and explaining WPT via magnetic resonance coupling, interest in WPT has increased [8]. Many groups have contributed to advancements in better understanding RIPT. In [14] the optimal ratio of planar spiral coil sizes in a MRC-WPT system was examined. That group reported that when comparing coil size and distance for efficiency, at closer distances, transmit ($T_x$) and receive ($R_x$) coils of similar size have higher efficiency than coils of mismatched size, but as separation distances increase, the efficiency of a small $R_x$ coil coupled with a larger $T_x$ coil is better than similarly sized coils. Other work has been performed to compare different coil geometries, such as planar circular spiral coils, square helical coils, and circular solenoid coils to demonstrate the effects of coil shape on efficiency with change in load and separation distance [15]. The results indicate that power transfer through planar spiral coils generally decreases more quickly due to deviations in operating

frequency, as opposed to other coil shapes. However, planar spiral coils perform similarly to other shapes when the operating frequency is close to the resonant frequency of the coils.

The concept of resonant capacitive coupling wireless power transfer to charge and power an aerial vehicle was illustrated in a brochure by Solace Power Inc. [16]. However, as mentioned, this technology is subject to the generation of potentially high voltages and unsafe electric fields. On the other hand, resonant inductively coupled coils, which are more robust and operate at lower voltages, have been demonstrated for WPT to a dynamic load [13]. In that work, researchers designed an inverter and rectifier specific to the load. Connected to that publication, a simple demonstration was performed to power an MAV quadcopter, in which the $T_x$ coil used was a clover-shape printed circuit and the $R_x$ coil was made of copper tape, which was wrapped around the quadcopter frame. However, the detailed design, modeling, and analysis of the inductive resonant WPT system specific to MAV operation, to best knowledge of the author, was not performed and published. A separate work details the design of a magnetic resonance coupled WPT system for a small remote controlled helicopter (6g), in terms of automatic impedance matching by changing the position of the $T_x$ driving loop with respect to the $T_x$ coil [17]. The researchers in that work attached the $T_x$ driving loop to a linear actuator and created a control loop designed to minimize reflected power at the source by moving the loop back and forth. The power received at the $R_x$ loop was rectified to DC but was not regulated to an appropriate voltage to enable the helicopter to operate through remote control. The helicopter was reported to have consumed 5W. This project presents new work on a detailed model-based approach to design a WPT, specifically for an MAV using a

commercial power amplifier with fixed output impedance, and experimentally demonstrates the system's ability to provide enough power to enable hovering.

# CHAPTER 3

# RESONANT INDUCTIVE COUPLING WIRELESS POWER TRANSFER

Many researchers have presented theories and models on inductive coupling, resonant inductive coupling, and magnetic resonance coupling. Current models used to simulate WPT systems include coupled mode theory [8], lumped circuit theory or circuit model theory [11], [18], [19], reflected load theory [20], and spherical mode theory [21]. One study of the three main modeling techniques (coupled mode, circuit model, and reflected load) indicates that they are equivalent in prediction of system performance [22]. In this work, circuit theory is used. The following chapter discusses the modeling approach for the WPT system, the main design output considerations for the problem, and the WPT system design parameters taken into consideration.

## 3.1 Circuit Theory on Resonant Inductive Coupling

A resonant inductive power transfer system consisting of two coils is dependent on the coupling coefficient, *k*, which characterizes the strength of the interaction between the coils. The coupling coefficient is proportional to the mutual inductance of the coils, *M*, by

$$k = \frac{M}{\sqrt{L_i L_j}}, \tag{3.1}$$

where $L_i$ is the inductance of the $T_x$ coil and $L_j$ is the inductance of the $R_x$ coil. Mutual inductance of two single loops is found using Grover's method[23], which is given by

$$\frac{M}{A} = \frac{1}{2\pi}\int_0^{2\pi} \frac{\left(\frac{m}{A}\right)\left[\cos(\theta) - \left(\frac{\rho}{a}\right)(\cos(\psi)\cos(\varphi) - \sin(\psi)\sin(\varphi)\cos(\theta))\right]}{\zeta^2} d\varphi \text{ abhenries,} \quad (3.2)$$

where $a$ is the radius of the smaller of the two loops, $A$ is the radius of the larger of the two loops, $\rho$ is the x displacement of the centers of the loops, $\varphi$ is the angle in the xy plane, $\theta$ is the rotation in the yz plane, and $\psi$ is the rotation in the xz plane. It is assumed that one loop will be placed in the xy plane. $\zeta$ is found using

$$\zeta^2 = (1 - \cos^2\varphi \sin^2\theta + 2\left(\frac{\rho}{a}\right)(sin\psi sin\varphi - cos\psi cos\varphi cos\theta) + \frac{\rho^2}{a^2}, \quad (3.3)$$

and $m/A$ is found using graphical charts found in [23]. An alternative to Grover's formula was developed and presented in [24]. To calculate the mutual inductance of the coils, the turns of each coil are treated as a single loop, so that a coil is modeled as a series of concentric loops. The mutual inductance of each loop of one coil is then calculated with respect to each of the loops of the opposing coil and summed.

The circuit used in this work and shown in Figure 3.1.c relies on Z-parameter analysis. The impedances of the first and second coils are represented by $Z_{Tx}$ and $Z_{Rx}$, respectively. The impedances of a coils are given by

$$Z_{T_x} = R_{T_x} + jwL_{T_x} + \frac{1}{j\omega C_{T_x}}, \quad (3.4)$$

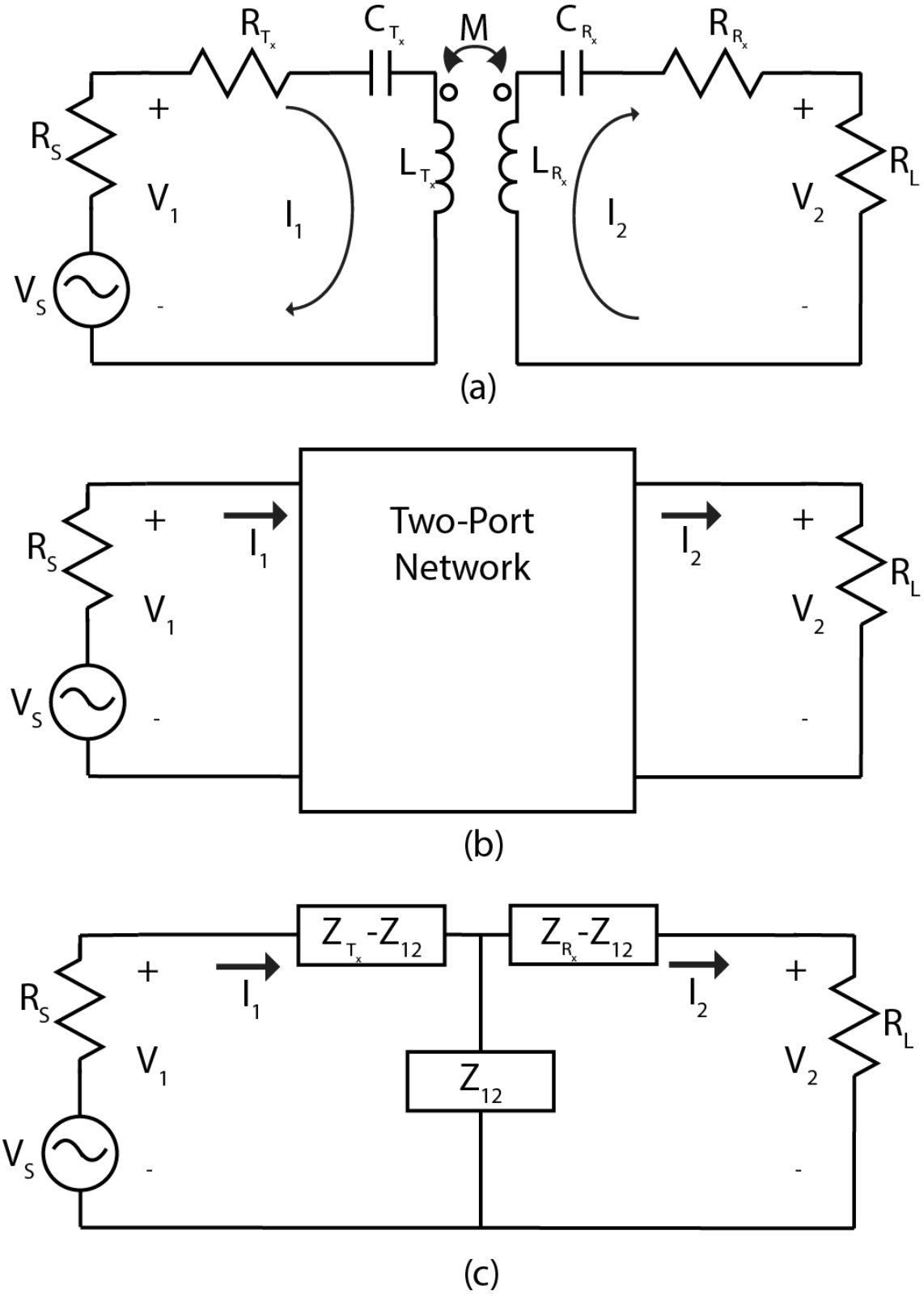


Figure 3.1: A two-port network is shown here, where (a) is the two-coil WPT system, (b) is a general two-port network, and (c) is a T-equivalent two-port network using Z-parameters.

$$Z_{R_x} = R_L + R_{R_x} + jwL_{R_x} + \frac{1}{j\omega C_{R_x}} . \quad (3.5)$$

The impedance of the interaction between the coils is represented by $Z_{12}$ or $Z_{21}$ and is given by

$$Z_{12} = Z_{21} = j\omega M . \quad (3.6)$$

The WPT system is represented as a two-port network, as shown in Figure 3.1.c. The impedance of the system as seen at the output of the amplifier and the impedance of the source and system as seen by the load are given by

$$Z_{in} = Z_{T_x} - \frac{Z_{12}^2}{Z_{R_x}}, \quad (3.7)$$

$$Z_{out} = Z_{R_x} - \frac{Z_{12}^2}{Z_S + Z_{T_x}} , \quad (3.8)$$

respectively. Given an output voltage of the power amplifier, the output current in the first and second coils can be calculated using

$$I_1 = \frac{V_S Z_{R_x}}{Z_{T_x} + (\omega M)^2}, \quad (3.9)$$

$$I_2 = -\frac{jV_S \omega M}{Z_{T_x} Z_{R_x} + (\omega M)^2}. \quad (3.10)$$

Average power received at the load, $P_L$, and average power delivered into the network, $P_{in,}$ are found with

$$P_L = \frac{1}{2}|R_L(I_2)^2|, \tag{3.11}$$

$$P_{in} = \frac{1}{2}V_S I_1 = \frac{\frac{1}{2}V_S^2 Z_{R_X}}{Z_{T_X}Z_{R_X}+Z_{12}}. \tag{3.12}$$

Using these power equations the efficiency is calculated with

$$\eta = \frac{P_L}{P_{in}} = Real\left(\frac{V_S^2(Z_{12})^2 R_L}{\left(Z_{T_X}Z_{R_X}+(Z_{12})^2\right)^2}\frac{\left(Z_{T_X}Z_{R_X}+(Z_{12})^2\right)}{\left(V_S^2 Z_{R_X}\right)}\right)\times 100. \tag{3.13}$$

With the detailed equations from circuit theory, it is now possible to properly simulate the behavior of a RIPT system.

## 3.2 Main Design Output Considerations for Resonant Inductive Coupling Theory

Generally the efficiency of the system is the primary output variable of interest. However, as is discussed in the Section 3.2, the main output of interest in this work is the figure of merit ($\chi$), the ratio of power received at the load to power required by the MAV to hover. In this work, the primary output of concern from the circuit theory is power at the load, $P_L$. For this work, it is important to maintain sufficient power with different misalignment distances, separation distances, and angular misalignments. Sufficient power is defined by the power required to lift the MAV and allow it to hover, which varies from one MAV to another. In this work, a consumer MAV is chosen and

characterized in Chapter 5.

## 3.3 Primary Parameter Considerations

In designing the WPT system, several parameters were considered in this work, which are discussed in the following sections, including frequency of operation, coil geometry and size, and coil material considerations. The analysis and discussion in this section explain why the final WPT system is made of two copper planar spiral coils operating at 13.56MHz.

### 3.3.1 Frequency

The Electronic Code of Federal Regulation defines several prohibited transmission frequencies to use, as well as several frequencies designated for Industrial, Scientific, and Medical (ISM) use [25]. The frequencies allowed in the ISM band include 6.78MHz, 13.56 MHz, 27.12MHz, 40.68MHz, and seven others up to 245GHz. In other works, 6.78MHz, 13.56MHz, and 27.12MHz are often used [13], [14], [20], [26]–[28]. The quality factor of a coil is given by

$$Q = \frac{\omega L}{R}, \tag{3.14}$$

where $\omega$ is the resonant frequency of a coil in radians per second, $L$ is the coil's self-inductance in Henries, and R is the coil's parasitic resistance in Ohms. With increasing frequency, the quality factor of the coil increases, which increases maximum efficiency of the system. Although efficiency is not the chief goal in this work, efficiency cannot be

set aside altogether due to safe human electromagnetic exposure limitations and power supply limitations. Operating frequency is also limited by components. Operating at higher frequencies often requires lower coil inductance in order to properly tune to resonate at the desired frequency. For this work, 13.56MHz was found to be suitable, but operating at 6.78MHz or 27.12MHz would also be possible.

### 3.3.2 Coil Size and Geometry

To determine a suitable coil size and geometry for this work, considerations include how the coil can be mounted to the MAV, how the system could work in an industrial or consumer setting, as well as the effects on power transmission and required MAV power due to coil geometry, coil diameter, and wire diameter. In [15], three separate coil geometries are considered for transmission efficiency: planar spiral, circular helix (solenoid), and square helix. The coils were all assumed to cover the same area and each system was made up of a four-coil system. It should be noted that the planar spiral coils were made with less wire length than either of the helix coil geometries. The circular helix coil geometry demonstrated consistent maximum power transfer efficiency (80-90%) over a range of loads. The square helix coils consistently demonstrated efficiency of approximately 80% with loads varying from the optimal load value. The planar spiral coil geometry demonstrated approximately 80% efficiency when the optimal load was considered, but fell to approximately 50% when the load was many times lower than the optimal load. Operating frequency was also varied, and it was found that the circular helix coils performed best. The power transfer efficiency was also compared with increasing separation between $T_x$ and $R_x$ coils. The planar spiral coil geometry performed similarly to both helix coils between one and three times the coil maximum diameter, and

performed better than the circular helix coil geometry for distances farther than three times the diameter.

Another comparison between different coil geometries was performed in [29]. Two-coil inductive links were used. Four different geometries were discussed, including solenoid circular coils, flat spiral coils, printed circular coils, and printed square coils. The planar spiral coils were reported to outperform the coupled solenoid coils in both increasing separation and lateral misalignment. The coupled circular spiral coils were shown to outperform both the planar circular coils and the solenoid coils in separation distance and lateral misalignment. The square printed coils performed similarly to the planar coupled coils.

Another consideration when choosing a suitable geometry is how the coil can be attached to the MAV and the potential uses in industrial or consumer settings. Circular solenoid coils can be wrapped around the MAV or hung from the frame, as can square solenoid coils. Planar coils can be attached under or on the arms of an MAV, and can also be hung from the MAV frame. Thus, the $R_x$ coil has several suitable geometries to attach to the MAV. The $T_x$ coil can also be made into any of the discussed geometries, but in industrial and consumer settings, it is assumed that flat coils are preferred because they can be more easily embedded into surfaces, and generally take up less volume. Therefore, due to the convenience of the $T_x$ coil placement, the reported performance of planar spirals compared to other geometries, and how the coil may be attached to an MAV, planar spiral coils were found to be suitable for this work.

The coil diameter is largely dependent on the size of the chosen MAV and the desired power transfer distance. Larger diameter coils result in greater transmission distance, in general. In [14], the ratio of $T_x$ coil size to $R_x$ coil size is examined and shown

that when the $T_x$ coil and $R_x$ coil have similar diameters, the power transfer is more efficient for distances approximately the diameter of the $R_x$ coil. However as the distance increases, larger $T_x$ coils coupled with smaller $R_x$ coils have a greater transfer efficiency than $T_x$ and $R_x$ coil combinations with similar diameters. Larger coil diameter also increases the mass of wire and can increase the MAV power required to hover. Wire diameter and length of wire used to make the coil become important when considering $\chi$ and the optimal resistance value. The optimal load and source resistance values are discussed in Section 3.4. The wire gauge used affects the efficiency because smaller gauge wire increases the resistance of the coils, and therefore reduces the power delivered to the load. However, the resistance of the coils can be used to adjust $Z_{in}$ and $Z_{out}$ and decrease the reflected power.

### 3.3.3 Material Considerations

Copper is most commonly used in WPT technologies due to the low cost, high availability, and high electrical conductivity. Aluminum is also used in electrical applications. Aluminum has conductivity approximately 61% that of copper, but is only 30% the density of copper. The lower density is beneficial for this work because it would require less energy for the MAV to carry an aluminum coil versus a copper coil of the same size. The additional resistivity of aluminum is detrimental to the power transfer and efficiency of the WPT system because Q factor decreases with increasing resistivity. Another problem with aluminum wiring is that soldering to aluminum is more difficult due to the rapid creation of aluminum oxide on the skin of aluminum. Preliminary testing with aluminum coils indicated that the added resistivity introduced excessive damping to the oscillating circuits and power transfer was dramatically reduced. While other

conductive materials can be used to construct WPT coils, such as silver or gold, copper is the best choice due to its conductivity and availability.

### 3.3.4 Two-Coil vs. Four-Coil WPT System

In literature, most two-coil systems are referred to as inductive power transfer systems, and most four-coil systems are referred to as magnetic resonance coupled systems. A four-coil system consists of two loops—a drive loop and a load loop—and two resonators, as shown in Figure 3.2. The work presented in [8] brought the four-coil system to light.

In this original four-coil system, the two loops were used as a way of adjusting $Z_{in}$ and $Z_{out}$ to improve power transfer efficiency of the system. By changing the distances between loop and coil, the coupling between loop and coil can be adjusted to improve system efficiency. This technique is also used in [17] to minimize reflected impedance as the load changes.

One of the argued advantages of the four-coil system is that the Q factor can be better than a two-coil system [30], which enables a higher efficiency and enables larger transmit distances from source loop to load loop. However, some argue that a two-coil system performs similarly to a four-coil system. In [12], Ricketts *et al.* demonstrate the similarities between two-coil and four-coil systems with varying coil diameters and over a range of frequencies. The work presented in [11] indicates that the main difference between a two-coil and four-coil system is how impedance matching is carried out. As discussed earlier, the four-coil system can match impedances by varying the separation between loop and coil. The two-coil system relies on other forms of impedance matching, such as L-networks, T-networks, or pi-networks. With proper impedance matching in

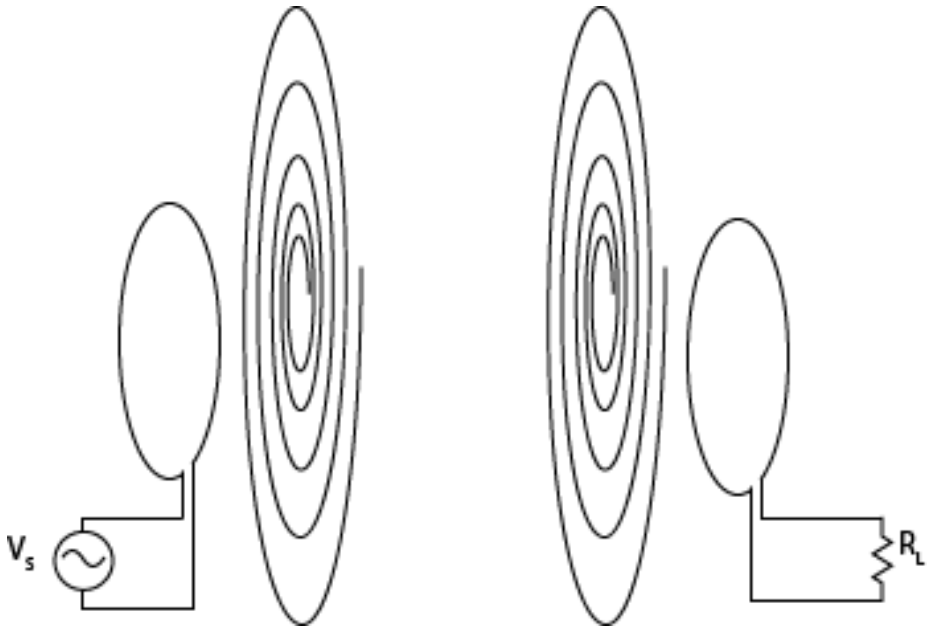


Figure 3.2: A four-coil system consisting of (from left to right) a drive loop, $T_x$ oscillating coil, $R_x$ oscillating coil, and a load loop.

place, the two-coil and four-coil systems perform equivalently. One of the advantages of a two-coil system is that it can be lighter on an MAV than a four-coil system because an $R_x$ coil without a load loop is all that is required.

### 3.3.5 Impedance Matching

As mentioned in the previous section, several forms of impedance matching exist, including L-networks, pi-networks, T-networks, and DC-DC converters [31]. Also mentioned above was the role of coil resistance to reduce reflected impedance. By correctly designing the resonators, $Z_{in}$ can be designed to match the source impedance of the power amplifier. This eliminates the need for impedance matching networks, which can be lossy and consume power. Impedance matching networks used on the MAV side increase the weight of the MAV payload. The derivation to determine the optimal

resistance values of the coils to avoid impedance matching networks can be explained by deriving optimal source and load resistance values.

The maximum power transfer occurs when

$$Z_{in} = Z_s, \tag{3.15}$$

where $Z_s$ is the source impedance of the power amplifier. In this work $Z_s$=$R_s$=50Ω. $Z_{in}$ is defined in Section 3.1 as

$$Z_{in} = Z_{T_x} - \frac{Z_{12}^2}{Z_{R_x}} = Z_{T_x} + \frac{(\omega M)^2}{Z_{R_x}}. \tag{3.16}$$

By substituting 3.15 into 3.16, and assuming that at resonance the capacitive and inductive components of the coils cancel, the optimal load resistance is found to be

$$R_{L_{opt}} = R_{R_x} + \frac{(\omega M)^2}{R_{T_x}+R_s}. \tag{3.17}$$

Similarly, the optimal source impedance value occurs when

$$Z_{out} = Z_L. \tag{3.18}$$

By assuming that the coils resonate at the resonant frequency and by using

$$Z_{out} = Z_L = Z_{R_x} - R_L - \frac{Z_{12}^2}{Z_{T_x}+Z_s} = Z_{R_x} - R_L + \frac{(\omega M)^2}{Z_{T_x}+Z_s}, \tag{3.19}$$

and solving for $Z_s$, the optimal source impedance value is found to be

$$R_{S_{opt}} = R_{T_x} + \frac{(\omega M)^2}{R_{R_x}+R_L}. \tag{3.20}$$

Substituting 3.20 into 3.17 yields

$$R_{L_{opt}} = \sqrt{{R_{R_x}}^2 + \left(\frac{R_{R_x}}{R_{T_x}}\right)(\omega M)^2}, \tag{3.21}$$

and the optimal source resistance value can be expressed as

$$R_{S_{opt}} = \frac{R_{T_x}}{R_{R_x}} R_L. \tag{3.22}$$

In this work, the values for the source and load resistances are known and fixed. $R_L$ is fixed because the load of interest is a quad-rotor MAV. An MAV is selected and characterized in Chapter 5, and the equivalent impedance of the MAV while hovering is found to be approximately 1Ω. With known $R_L$ = 1Ω and $R_S$=50Ω the optimal value for $T_x$ and $R_x$ resistances can be found as

$$R_{T_{x_{opt}}} = \frac{R_S}{R_L} R_{R_x} \tag{3.23}$$

and

$$R_{R_{x_{opt}}} = \pm \frac{\sqrt{R_L R_S (R_L R_S - (\omega M)^2)}}{R_S}. \quad (3.24)$$

Using equations 3.23 and 3.24, the WPT system can be designed to prevent the need for matching networks. In practice, it may be difficult to construct coils with the exact resistance values, and load or source impedance values may not be exactly as expected, so some additional impedance matching may be necessary. DC-DC converters have been used to match impedances[31], [32] and are used in this work to regulate the voltage delivered to the MAV.

## 3.4 Planar Circular Spiral Coil Modeling

To properly model the chosen planar coils the components of the coils, such as capacitance, inductance, and resistance, must be determined in the model. A frequency of 13.56MHz has been determined as suitable for this work, which is needed to calculate the modeled components. The component calculations have been performed in [14].

### 3.4.1 Inductance

Inductance is determined using a modification of Wheeler's formula. The inputs for the inductance calculation are the number of coil turns ($N$), the outer diameter of the coil ($D_o$), the wire diameter ($w$), and the coil pitch ($p$), which is defined as the distance from edge to edge between wire turns. The inductance calculation is made using

$$L(H) = \frac{N^2\left(D_o - N(w+p)\right)^2}{16D_o + 28N(w+p)} \times \frac{39.37}{10^6}. \quad (3.25)$$

### 3.4.2 Capacitance

The self capacitance of a coil is reliant on the number of turns, pitch, and the wire diameter. Self capacitance of a coil is typically on the order of a few pF, and is generally considered negligible. To determine the needed tuning capacitance to add to coil frequency (*f*) is needed, as well as the previously calculated inductance (L). The tuning capacitance value is calculated using

$$C(F) = \frac{1}{(2\pi f)^2 L}. \quad (3.26)$$

While it is common to neglect the self capacitance of the coil, as the number of coil turns increases the capacitance between coil turns also increases. With increased coil turns, the inductance also increases, and the required tuning capacitance decreases. The increased capacitance between coil turns can then become significant. Therefore, as coil turns increase, the calculated tuning capacitance becomes less accurate. However, it can still be used to estimate the required capacitance value. In practice, it is recommended that capacitance be added to obtain the correct resonant frequency.

### 3.4.3 Resistance

Coil resistance is made of two different forms of resistance. The first is DC resistance, which can be measured using an Ohm meter. The second form is radiative resistance, also known as AC resistance. Radiative resistance occurs in antenna

applications. Energy lost due to radiation is seen by the source as resistance [33]. To calculate resistance values, the conductivity of the coil material ($\sigma$), permeability of free space ($\mu_0$), and wire diameter ($w$) must be known. In this work, the coil material is copper. The conductivity of copper is $\sigma$=59.6×10$^6$ $\frac{S}{m}$, and the permeability of free space is $4\pi \times 10^{-7}\,\frac{H}{m}$. The DC resistance can be calculated using

$$R_{DC}(\Omega) = \frac{1}{\sigma\pi(\frac{w}{2})^2}. \tag{3.27}$$

The AC resistance calculation requires the skin depth (δ) in addition to previously defined variables. Skin depth is calculated with

$$\delta(m) = \frac{1}{\sqrt{\pi f \sigma \mu_0}}, \tag{3.28}$$

and the calculation for the combined resistance is made with

$$R(\Omega) = \frac{R_{DC} w}{4\delta} = \sqrt{\frac{\pi f \mu_0}{\sigma}} \times \frac{wN(D_o - N(w+p))}{8D_o + 14N(w+p)}. \tag{3.29}$$

The calculations for inductance, capacitance, and resistance presented in equations 3.25-3.29 are used to determine the impedance of the $T_x$ and $R_x$ coils, and the impedance of the overall system from Section 3.1.

# CHAPTER 4

# WIRELESS POWER TRANSFER SYSTEM VALIDATION

With the model of the WPT system compiled, it is necessary to validate the results. In this section, the experimental setup and procedure is explained in which model results are validated.

## 4.1 Test Setup and Procedure

To validate the model, several coils were constructed. A $T_x$ coil was constructed using 14 AWG solid core copper wire, consisting of seven turns and 5 mm pitch. The outer coil diameter is 190 mm. Figure 4.1 shows the coil. Also constructed were two $R_x$ coils shown in Figure 4.2. Both coils are made using 16AWG wire (1.23mm diameter). The first coil has an outer diameter of 137mm, and consists of two turns and a 1mm pitch. The second coil has an outer diameter of 153mm, and consists of four turns and a 2mm pitch.

A 13.56MHz power amplifier built by WiBotic, Inc. with an output impedance of 50 Ω was used to power the WPT system. The amplifier is connected using BNC cables to an SWR/Wattmeter to monitor forward and reflected power. The $T_x$ coil is then connected, also using BNC cables. The $T_x$ coil is placed flat on a tabletop. The $R_x$ coil is placed flat on a raised acrylic platform. A resistive load is used to evaluate power transfer. Figure 4.3 shows a picture of the entire test setup.

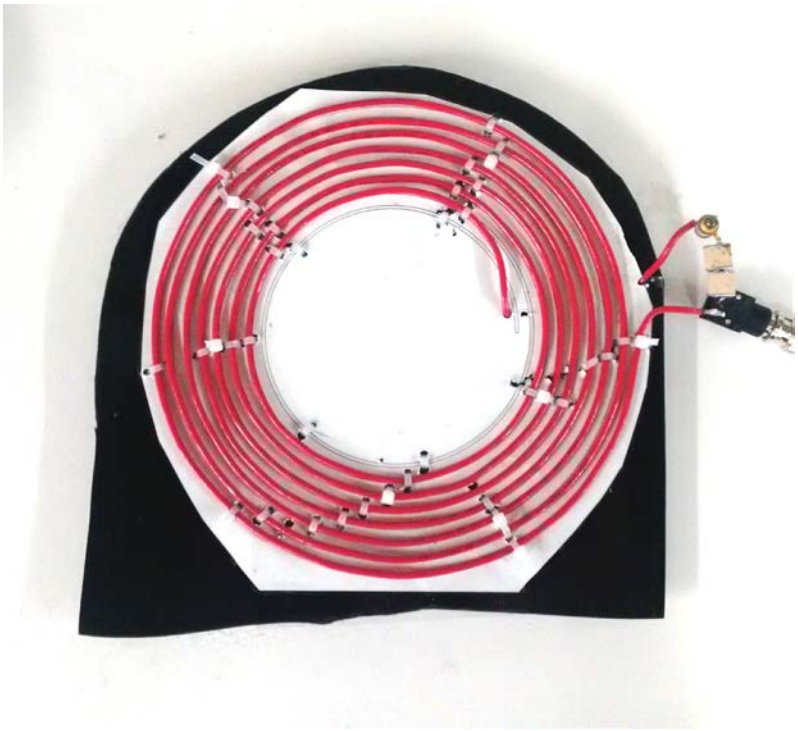

Figure 4.1: A picture of a $T_x$ coil used in the experimental validation. The outer diameter is 190mm, the pitch is 5mm, and the wire diameter is 1.63mm (14AWG).

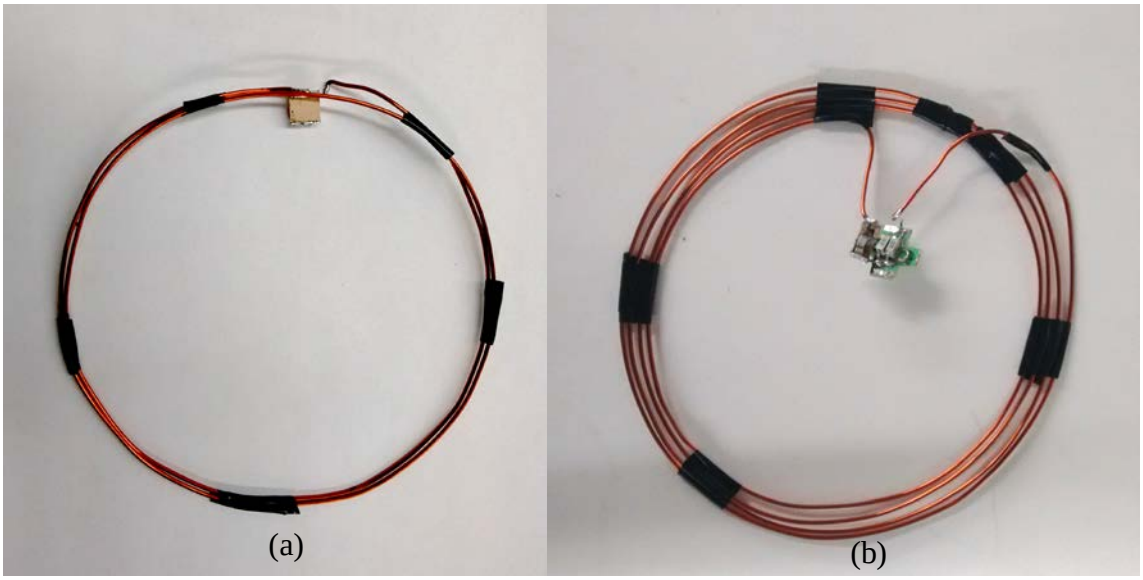


Figure 4.2: A picture of two different $R_x$ coils is shown here. The first coil (a) has an outer diameter of 137mm, a pitch of 1mm, and is made with two turns. The second coil (b) has an outer diameter of 153mm, a pitch of 2mm, and is made of four turns. Both coils are made using 16AWG (1.29mm) wire.

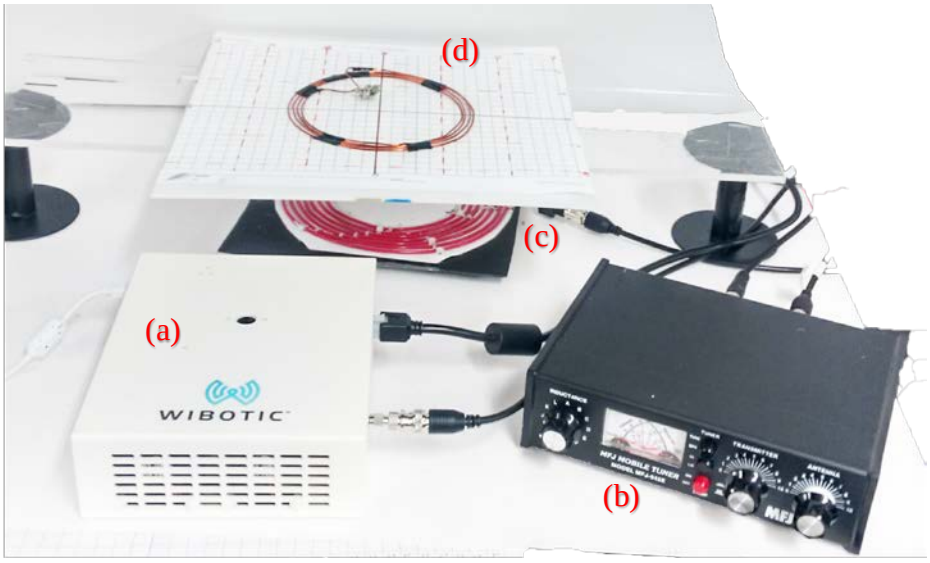


Figure 4.3: A picture displaying the test setup with (a) the WiBotic, Inc. power amplifier, (b) the SWR/Wattmeter, (c) the $T_x$ coil, (d) and the $R_x$ coil.

Power delivered to the system is measured using the SWR/Wattmeter by subtracting the indicated reflected power from the indicated forward power. The $P_{in}$ is also measured and confirmed using the output of the GUI for the power supply. Power delivered to the load is measured by measuring the sinusoidal voltage across the resistive load using an oscilloscope and calculating the RMS voltage. The RMS voltage is used to calculate the power delivered to the load with

$$P_L = \frac{V_{RMS}^2}{R_L}. \tag{4.1}$$

The $R_x$ coil was placed on a surface 100mm directly above the $T_x$ coil and the power was measured. The inductance of the coils were measured. The resonant frequency of the coil was measured by applying a sinusoidal voltage to the coil and added capacitance, then measuring the voltage across the coil. The frequency is varied and the

change in voltage is noted. At the resonant frequency, the inductive and capacitive elements of the coil equally counteract and the voltage dips. The total coil capacitance is found by using equation 3.26. The results of the experiments are shown in Table 4.1.

The efficiency of the WPT system was also measured with varying coil axial misalignment. $R_x$ coil 1 was placed directly above the $T_x$ coil and moved incrementally horizontally away from axial alignment. At each step, $P_{in}$ and $P_L$ were measured. The resulting efficiencies are shown in Figure 4.4.

## 4.2 System Characterization

To demonstrate the accuracy of the model, the results as shown in Section 4.1 are compared to theoretical values obtained from the modeled equations and presented in Table 4.2, Table 4.3, and Table 4.4. Generally the model provides accurate predictions of system performance. The largest deviation between theoretical and experimental values is the power at the load of the 157mm coil in Table 4.4. In future work, it would be beneficial to calculate power transfer and efficiency using measured values of inductance,

Table 4.1: Experimental values obtained for different $R_x$ coils and the 190mm outer diameter $T_x$ coil, with a coil separation of 100mm.

| | **$R_x$ Coil 1** | **$R_x$ Coil 2** |
|---|---|---|
| **N** | 2 | 4 |
| **Pitch(mm)** | 1 | 2 |
| **$D_o$(mm)** | 137 | 153 |
| **L(μH)** | 1.4 | 4.6 |
| **C(pF)** | 103.2 | 29.9 |
| **$f_o$(MHz)** | 13.24 | 13.27 |
| **$R_L$(Ω)** | 12.5 | 12.5 |
| **$P_{in}$(W)** | 18 | 16 |
| **$P_L$(W)** | 15.2 | 9 |

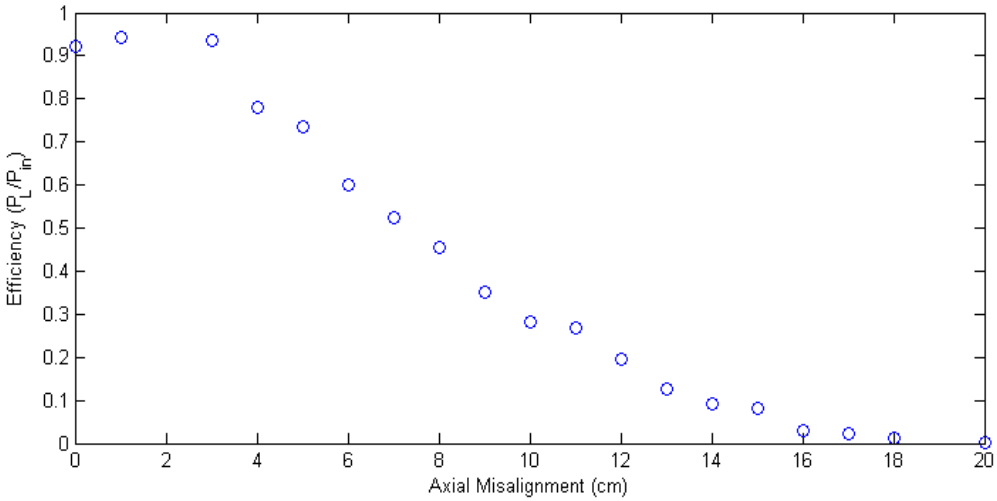


Figure 4.4: The relationship between efficiency and axial misalignment using $R_x$ coil 1 and a 12.5Ω load is shown. There is noticeably a small area near the center of the $T_x$ coil where the efficiency is fairly constant. This is expected to be due to the slightly smaller $R_x$ coil compared to the $T_x$ coil diameter.

Table 4.2: Theoretical vs. experimental values are listed in this table for the $T_x$ coil.

| | **Theoretical** | **Experimental** | **% Deviation** |
|---|---|---|---|
| $\mathbf{N_{T_x}}$ | 7 | 7 | - |
| **Pitch (mm)** | 5 | 5 | - |
| $\boldsymbol{D_{o_{T_x}}}$**(mm)** | 190 | 190 | - |
| $\mathbf{L_{T_x}}$**(μH)** | 9.17 | 10.67 | 15.1 |
| $\mathbf{C_{T_x}}$**(pf)** | 15.03 | 12.85 | 15.6 |
| $\boldsymbol{f_o}$**(MHz)** | 13.56 | 13.59 | 2.2 |

capacitance, and resonant frequency to obtain more accurate theoretical values. The model is quite accurate for the two-turn coil, as shown in Table 4.3. The largest deviation between experimental and theoretical values is the inductance. It can be seen in Figure 4.2 that the spacing is not uniform between coil turns. This will affect the inductance of the coil and inherently the capacitance. However, even with these differences, the percentage deviation of the power delivered to the load is 11.1%.

Table 4.3: The theoretical and experimental values are shown in this table for the 13.7cm $R_x$ coil. The power values here are found using the $T_x$ coil as detailed above.

| | **Theoretical Values** | **Experimental Values** | **% Deviation** |
|---|---|---|---|
| $\mathbf{N_{R_x}}$ | 2 | 2 | - |
| **Pitch (*mm*)** | 1 | 1 | - |
| $\boldsymbol{D_{o_{R_x}}(mm)}$ | 137 | 137 | - |
| **Coil Separation** | 100 | 100 | - |
| $\boldsymbol{R_L(\Omega)}$ | 12.5 | 12.5 | - |
| $\mathbf{L_{R_x}}(\boldsymbol{\mu})$ | 1.19 | 1.4 | 16.2 |
| $\mathbf{C_{R_x}}(\boldsymbol{pF})$ | 115.7 | 103.2 | 11.4 |
| $\boldsymbol{f_o(MHz)}$ | 13.56 | 13.24 | 2.4 |
| $\boldsymbol{P_L(W)}$ | 16.91 | 15.2 | 10.65 |
| $\boldsymbol{P_{in}(W)}$ | 18.07 | 18 | 0.39 |
| $\boldsymbol{\eta}$ **(%)** | 94.3 | 84.4 | 11.1 |

The comparison between theoretical and experimental results of the 15.3cm $R_x$ coil is shown in Table 4.4. The deviation is greater for this coil. Similar to the 13.7cm coil, the largest deviation between results is the power received at the load. If the measured values are used in the model, the theoretical power received at the load becomes 15.26W, which results in a percentage deviation of 51.6%. The large deviation could be due to differences in theoretical and actual coil resistances. In [18], Sample *et al.* presented resistance values that deviated by up to 144%. Neither the manner of measuring resistance experimentally, nor the specific modeling approach to calculate coil resistance were detailed, but later the research group presented an approach to model resistance of a coil [14], which is the method used in this work. Experimental coil resistances, which are higher than predicted resistance values, cause lower experimental efficiencies compared to theoretical efficiencies.

In this section, the model was shown to predict the actual performance of a WPT system with reasonable accuracy. It is noted that the coil with fewer turns better matches

Table 4.4: Theoretical and experimental values are compared in this table for the 15.3cm $R_x$ coil.

| | **Theoretical Values** | **Experimental Values** | **% Deviation** |
|---|---|---|---|
| $N_{R_x}$ | 4 | 4 | - |
| ***Pitch (mm)*** | 2 | 2 | - |
| $D_{o_{R_x}}(mm)$ | 153 | 153 | - |
| ***Coil Separation (mm)*** | 100 | 100 | - |
| $R_L(\Omega)$ | 12.5 | 12.5 | - |
| $L_{R_x}(\mu)$ | 4.4 | 4.6 | 4.4 |
| $C_{R_x}(pF)$ | 31.5 | 29.9 | 5.4 |
| $f_o(MHz)$ | 13.56 | 13.27 | 2.2 |
| $P_L(W)$ | 15.33 | 9 | 52.0 |
| $P_{in}(W)$ | 16.00 | 16 | 0 |
| $\eta$ **(%)** | 95.8 | 56.25 | 52.0 |

the theoretical results. For this work, it would be ideal to have fewer turns on the MAV to reduce the payload of the MAV. In the next chapter, suitable coil geometries are discussed and determined for use with an MAV. In this section, it was determined that more accurate predictions of system performance can be found if coils are built and coil inductance and capacitance determined experimentally, and these experimental values be used in the predictive model.

# CHAPTER 5

# DESIGN OF RESONANT INDUCTIVELY COUPLED WPT SYSTEM FOR AN MAV

Having verified the model, the next step is to design a WPT system that is suited for use with an MAV. In this chapter, the design approach is discussed when an MAV is present. A parameter sensitivity analysis is performed to investigate how design parameters affect the expected performance of the MAV. An explanation of the decision process is also included to justify a suitable prototype.

## 5.1 Design Explanation

The driving factor of WPT system design in this work is power density delivered to the MAV, or more specifically, the figure of merit, $\chi$. Efficiency is not the primary concern in this work, although the efficiency of the system cannot be completely neglected due to power supply limitations. To reiterate, $\chi$ is defined as the ratio of power received by the load (i.e. the MAV) versus the power required to lift the MAV, as shown in equation 1.1.

This work differs from other works primarily in the use of $\chi$. In most prior works, the primary concern is maximizing efficiency of the WPT system. The importance of $\chi$ is that it takes into consideration specific MAV power requirements. In other works involving an MAV, no consideration of the MAV maximum payload was considered. The logical goal in considering the MAV characterization is to provide the MAV with as

much power as possible with the shortest wire length to construct the coil.

## 5.2 Design Parameter Sensitivity Analysis

Many design parameters exist when designing a WPT system. These include coil shape, coil size, wire diameter, number of coil turns, coil pitch, operating frequency, power amplifier selection, impedance matching needs, material considerations, and the number of coils used. Many of these considerations were discussed in Chapter 3. Several parameters are examined to determine how some of these parameters affect power transfer with change in distance and misalignment. The parameters that will be examined are $R_x$ coil size (diameter), pitch, number of turns, wire diameter, operating frequency, and material considerations. For these simulations the $T_x$ coil is constant. The $T_x$ coil is made of seven turns, 1.63mm diameter copper wire with a 190mm outer diameter and 5mm pitch. Default parameters for the WPT system are defined for all simulations performed in the sensitivity analysis study and are included in Table 5.1. The simulations were performed with a maximum limit for voltage and current from the power supply, which are similar to the limits of the RF power supply used in this work. The figure of merit, $\chi$, is calculated in each plot using equation 1.1, which for convenience is shown below,

$$\chi = \frac{P_L}{P_{req}}, \tag{5.1}$$

where $P_L$ is the power delivered to the load as derived in Chapter 3, and $P_{req}$ is the power required by the MAV to lift the added weight of the coil. The characterization to determine

Table 5.1: A table indicating the default parameters used in the sensitivity study.

| Parameter | Value |
|---|---|
| $R_x$ Outer diameter (mm) ($d_o$) | 137 |
| $R_x$ Number of turns ($N_{Rx}$) | 2 |
| $R_x$ Wire Diameter (mm) ($wd_{Rx}$) | 1.29 |
| $R_x$ Pitch (mm) ($Pitch_{Rx}$) | 1 |
| Operating Frequency (MHz) (freq) | 13.56 |
| Wire Material | Copper |
| Axial Misalignment (mm) | 0 |
| Coil Separation (mm) | 150 |
| $V_{in}$ (V) | 50 |
| $I_{in}$ (A) | 2 |
| $R_L$ (Ω) | 1 |
| $R_s$(Ω) | 50 |

the relationship between power consumption and payload is detailed in Section 5.3.

The plot in Figure 5.1 indicates that a change in critical coupling accompanies change in coil diameter. As the $R_x$ coil changes, distance from the $T_x$ coil the coupling changes. A critical coupling value occurs at which the highest power transfer is achieved [34], and the highest χ is expected. The critical coupling value can be found using

$$k_{critical} = \frac{1}{\sqrt{Q_{T_x} Q_{R_x}}}. \tag{5.2}$$

As shown in equation 3.14, the Q factor is proportional to frequency and inductance, and inversely proportional to resistance. If inductance increases faster than resistance in a coil, the Q factor will increase and the critical coupling, $k_{critical}$, will decrease. With increasing distance coupling generally decreases. Therefore, for a larger diameter coil, $k_c$ is expected to be smaller and is achieved in the WPT system with a larger separation distance. The plot suggests that for any given coil diameter an optimal separation distance exists to

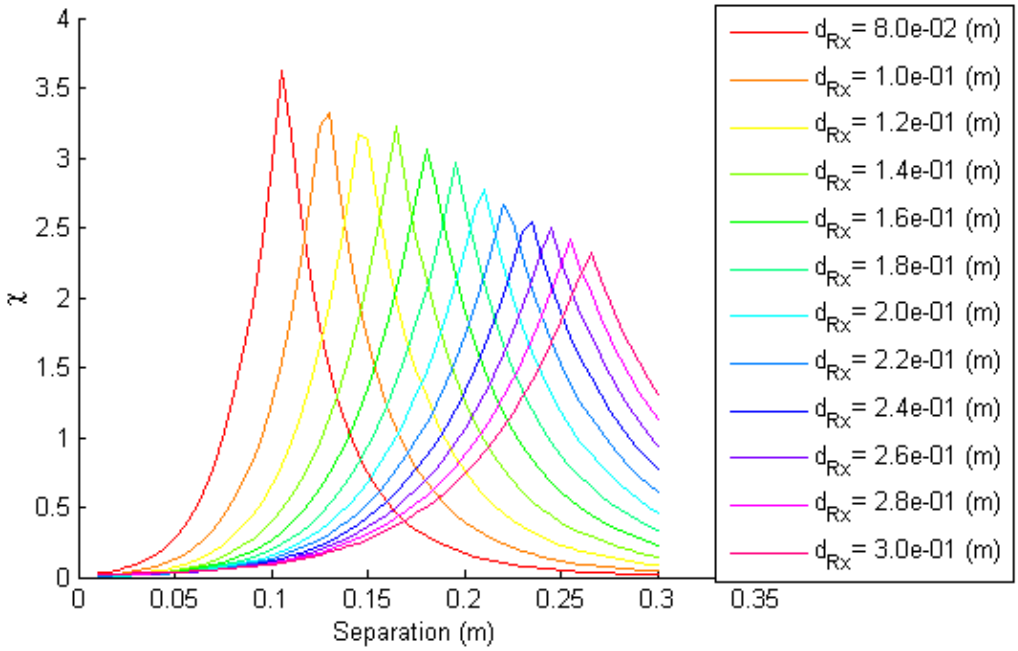


Figure 5.1: Theoretical changes in $R_x$ ($d_{Rx}$) diameter affect χ with changing separation distances are shown. The plot suggests that to achieve the highest χ at a given separation a coil diameter approximately equal to the separation distance should be used.

maximize χ.

From Figure 5.2 some splitting behavior is seen when simulating the effect of $R_x$ coil diameter on χ with alignment. Splitting occurs when the RIPT coils are over-coupled. To maximize χ when splitting occurs, the coupling coefficient, $k$, must be decreased. Coupling generally decreases with increasing distance and, as seen in this figure, greater misalignment. This plot suggests that the best coil diameter at the given parameters would be between 12cm and 14cm in diameter. A 14cm diameter in this simulation would work well for an MAV because χ is above 1 for a larger area.

The plot in Figure 5.3 also displays some splitting behavior. In this example, Q factor is affected by frequency, which affects $k_c$. For a given frequency, $k=k_c$ when χ

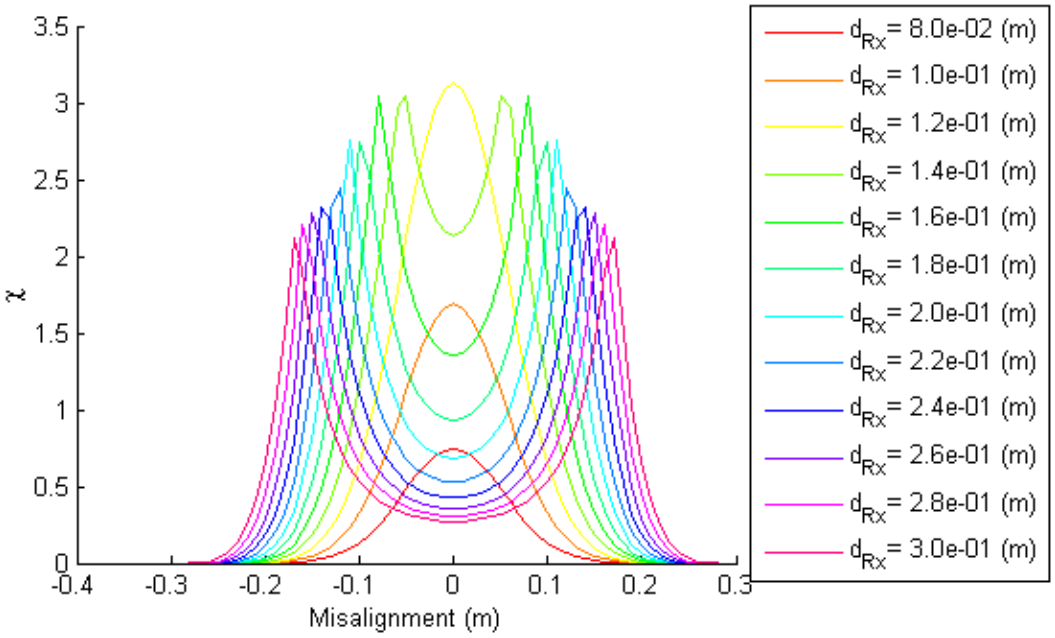


Figure 5.2: Changes in $\chi$ due to changing outer $R_x$ coil diameter and axial misalignment are shown. This plot displays some splitting behavior as coil diameters increase in size.

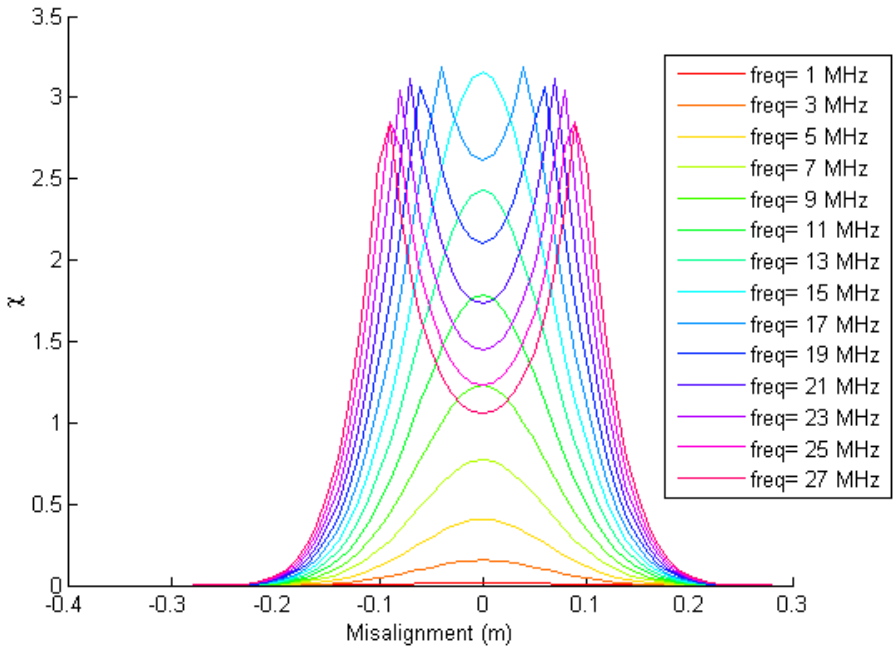


Figure 5.3: Frequency effects on $\chi$ due to changing misalignment. This plot suggests that an optimal frequency exists given a coil misalignment and fixed WPT parameters to maximize $\chi$.

peaks. The plot suggests that for the fixed separation, the best frequencies to operate the system are between 13MHz and 17MHz. In this work, frequency choices are limited by federal regulation and by RF power amplifier frequency limitations.

The simulation results shown in Figure 5.4 indicate that for a constant coil geometry, when the $T_x$ and $R_x$ coils are axially aligned, higher frequencies can cause $\chi$ to peak at greater separations than lower frequencies. This is caused by the Q factor. As seen in equation 3.14, if inductance and resistance of a coil is held constant and frequency is increased, Q factor will also increase. Q factor affects critical coupling, which affects the maximum power transfer in the WPT system. As the coils move farther apart, the coupling changes, and at certain distances, coupling is matched to the critical

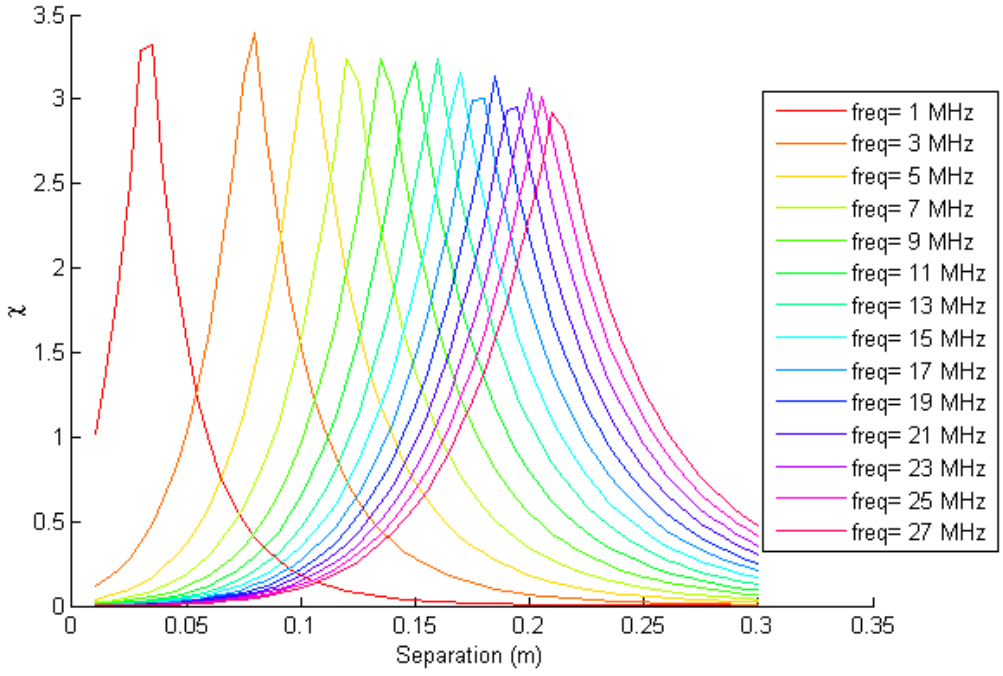


Figure 5.4: The effects of frequency on $\chi$ as coil separation changes are shown. The results of this plot indicate that there is an optimal separation distance at a given frequency.

coupling given a single frequency. A side note is that, according to the plot, higher frequencies have more similar performance to each other with varying distance than lower frequencies.

Different materials were considered with varying alignment and separation, and it was found that between three common materials, copper, aluminum, and silver, the performance was very similar. $\chi$ was very closely matched between all three cases. This is likely because $\chi$ takes into consideration both mass and power transfer. Therefore, although aluminum generally will have less power transfer than copper due to decreased electrical conductivity, the density of aluminum is lower than copper, and therefore, $\chi$ is very similar between the two. Silver has a slightly higher electrical conductivity than copper but also has a higher density. Therefore, $\chi$ is approximately the same for all three materials considered in this work.

The results from Figure 5.5 suggest that to achieve the highest $\chi$ with the given separation and coil parameters identified in Table 5.1, two to three $R_x$ coil turns should be used. The plot displays splitting behavior as the coupling changes with more coil turns. With changing coil turns, $k_c$ also changes. As alignment changes, $k$, also changes. As in cases from above, $k=k_c$ when peaks occur in the plot.

The results shown in Figure 5.6 suggest that for smaller distances, fewer $R_x$ coil turns cause higher $\chi$ when compared to more turns at greater distances. If the operating distance of the MAV is desired to be farther, then it is possible to add more turns to the coil and have a possibility of being able to operate under conditions when $\chi$ is greater than 1. The change in $k$ and $k_c$ is seen in this graph, as well.

The simulation results in Figure 5.7 suggest that the choice of wire diameter is not as critical to $\chi$ with changing alignment as other design parameters. Changing wire

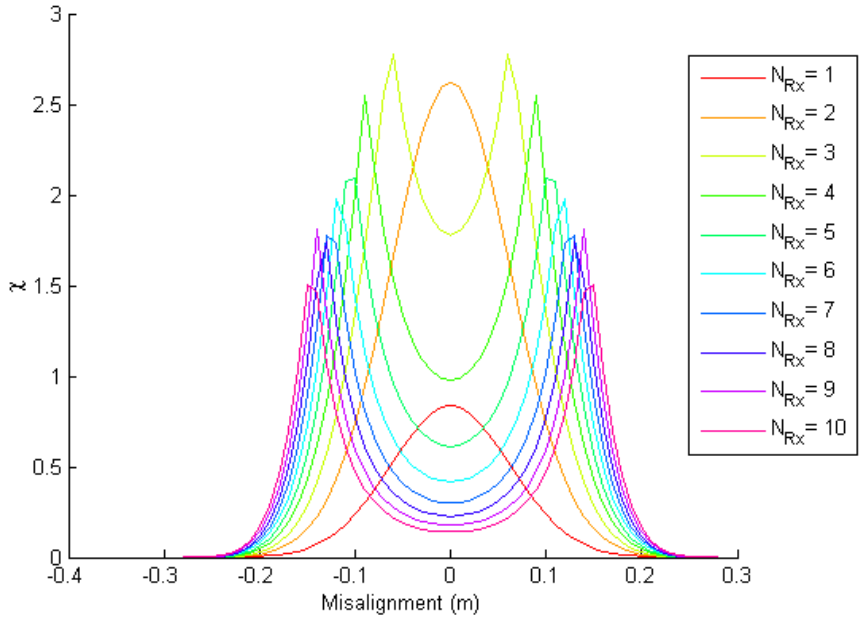


Figure 5.5: A demonstration how changing the number of $R_x$ coil turns affects $\chi$ as axial alignment changes. Splitting behavior is again observed as coupling changes with axial alignment. The plot suggests that for this simulation two to three coil turns achieves the highest $\chi$.

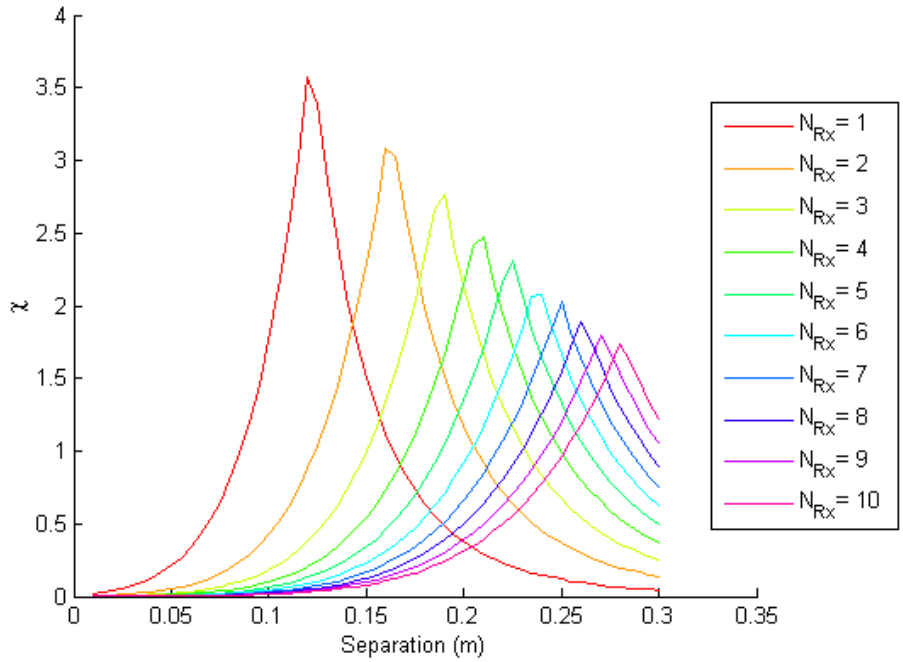


Figure 5.6: Changes to $\chi$ with different number of $R_x$ coil turns and changing separation. For each separation distance, there is an ideal number of turns; however, with more turns, $\chi$ decreases.

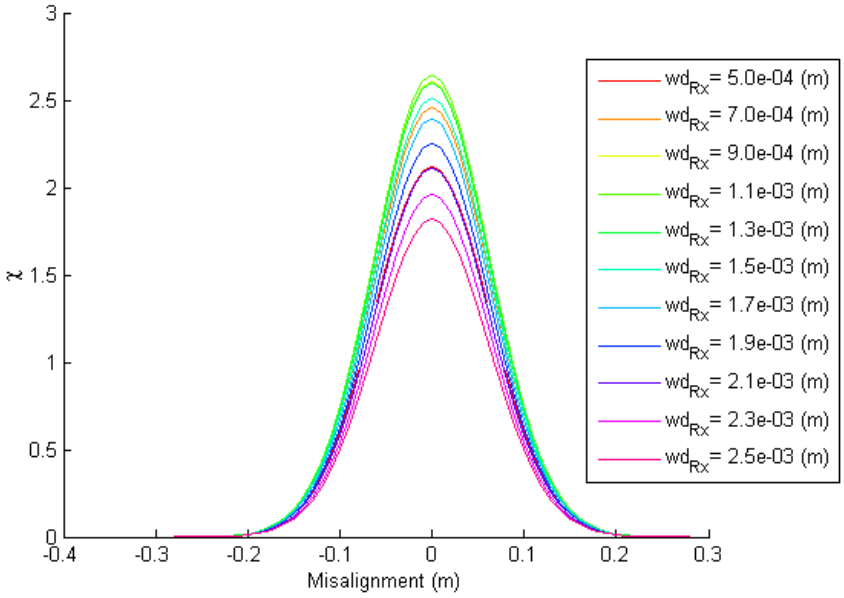


Figure 5.7: Differences in χ due to axial alignment changes using different wire diameters. While some wire diameters achieve higher χ, all drop off at a similar rate as axial misalignment increases.

diameter mostly affects the resistance of the coil, as seen in equations 3.27 and 3.29. As such, this plot exhibits that there is an optimal resistance related to wire diameter to achieve high χ. In all other graphs, the ascending order of design parameter values mapped to the magnitude of alignment at which χ peaked. In this case, all wire diameters have a peak χ at perfect alignment, but maximum χ occurs somewhere between 1.1mm and 1.3mm wire diameter. This occurs because the optimal resistance ratio is achieved, as discussed in Section 3.3.5 and shown in equations 3.23 and 3.24.

As in Figure 5.7, Figure 5.8 shows that changing wire diameter does not have as large an effect on χ as other design parameters. With changing coil separation, the maximum χ remains fairly consistent for different $R_x$ wire diameters. The largest effect on the RIPT system caused by changing wire diameter is the coil resistance. As explained above, the optimal values of $R_x$ resistance appears to occur when the wire diameter is

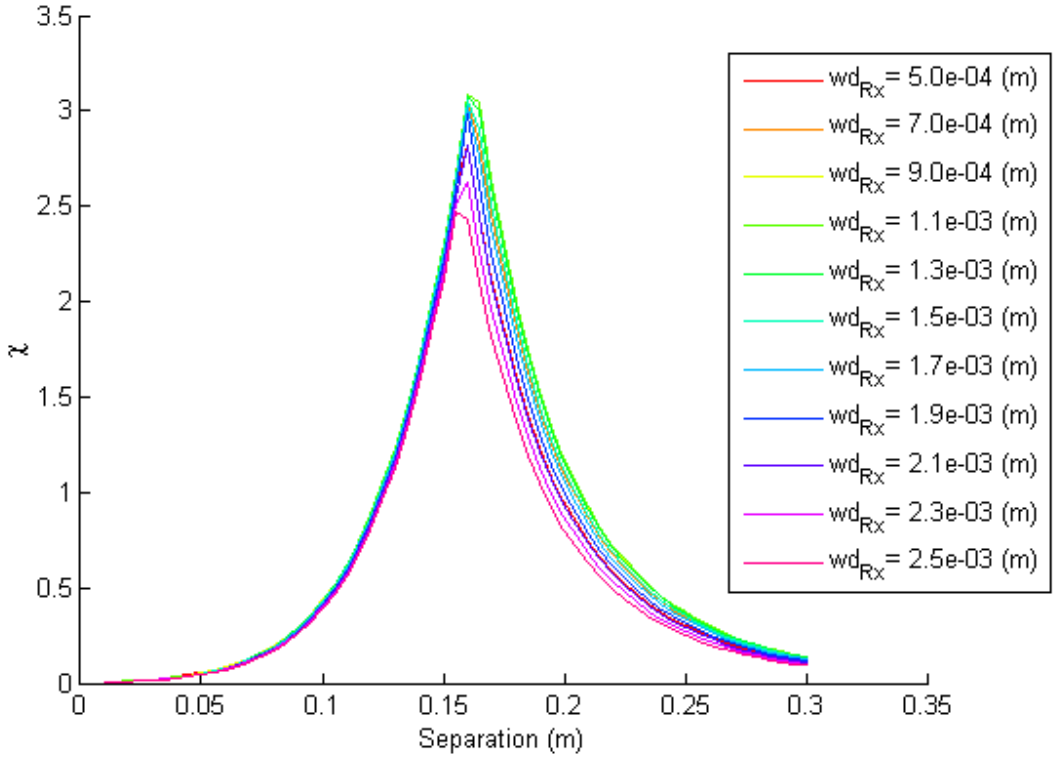


Figure 5.8: The effects of wire diameter on χ with changing coil separation. Wire diameter does not have as much of an effect on χ with different separations as axial misalignment does, but it appears that the best wire diameter to use for in this simulation would be between 1.1mm and 1.3mm.

between 1.1mm and 1.3mm. It is also noted that resistance is inversely proportional to Q factor and will therefore affect coupling. However, the change in resistance apparently does not largely affect coupling.

In Figure 5.9, it is shown that pitch has a large effect on χ. At perfect alignment, the best pitch occurs at 0mm pitch. In other words, tighter wound coils result in larger χ. Pitch affects both inductance and resistance. Tighter pitch requires more wire, which results in higher inductance and higher resistance. Tighter pitch also allows greater flux to be captured by the coil, as the capture area is greater. Overall the plot suggests that the coupling closest to critical coupling occurs with a tighter pitch.

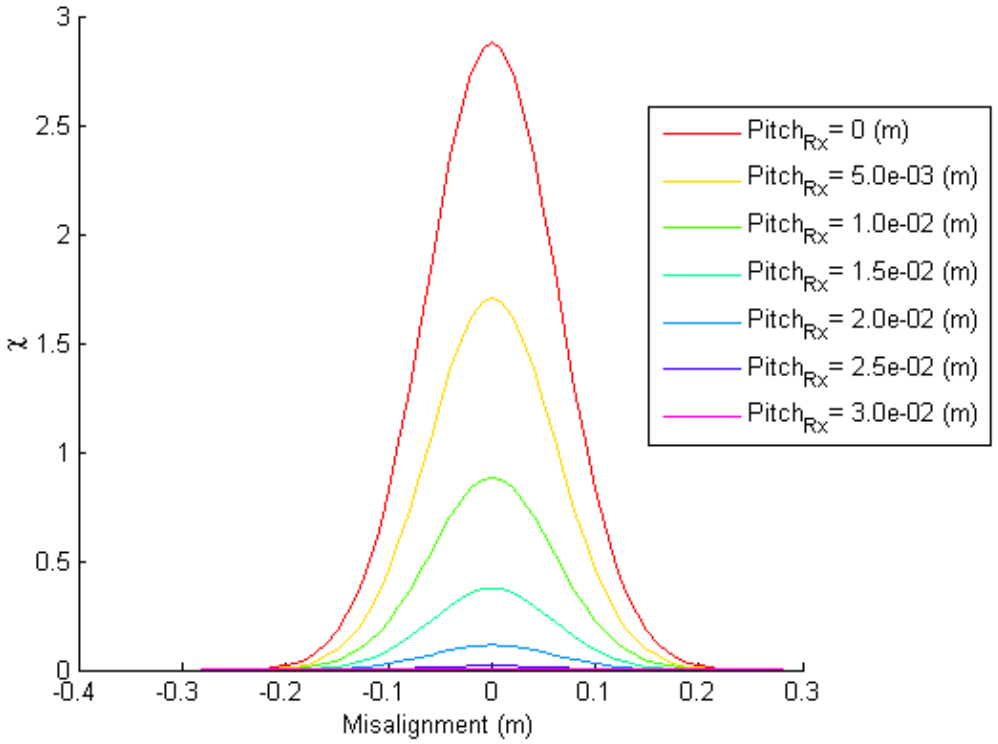


Figure 5.9: Changes in $R_x$ pitch and misalignment as it affects χ. As pitch changes χ changes drastically with and without misalignment. There is a noticeable difference in χ with changing pitch even at perfect axial alignment. At extreme misalignment all pitch sizes perform similarly.

A small pitch is needed to achieve high χ at larger distances, according to the results shown in Figure 5.10. The plot shows that as pitch increases, χ decreases. The coupling changes due to changes in resistance, inductance, and amount of magnetic flux captured.

Figures 5.1-5.10 are plots indicating how the design parameters effect χ with changing axial alignment and coil separation. In several plots, splitting behavior is seen. This splitting behavior occurs because with changing separation or axial alignment the coupling coefficient changes. As coupling coefficient changes, the effective impedance as seen by the power supply also changes. With a simulated limit on the RF power supply

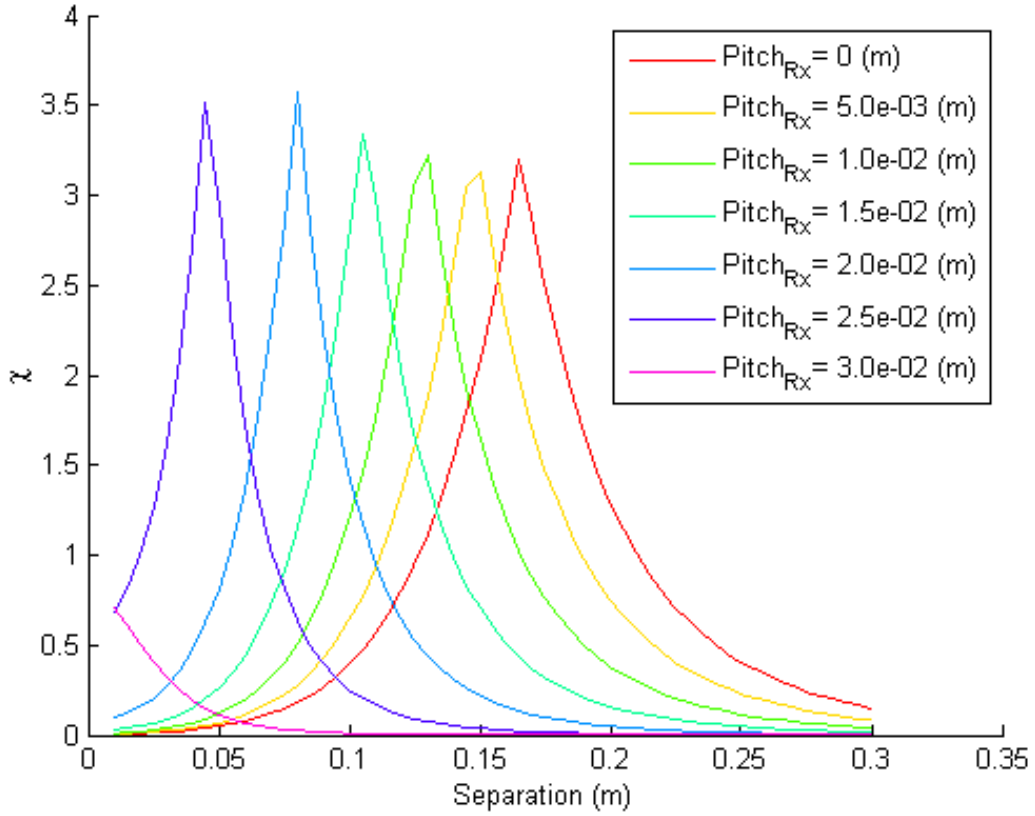


Figure 5.10: The effect of pitch on χ as separation changes. It appears that in this simulation a very close pitch will result in the largest separation distance.

the power reaches the maximum limit at the peak of each line, then decreases as the effective impedance of the WPT system changes. This phenomenon of splitting behavior is not unique to this work. It is also seen and discussed in [18] and [34].

According to the results from the preceding plots, the results from the sensitivity study indicate that as separation distance increases and as misalignment increases, more coil is generally needed by way of one or more parameters. For example, increasing the number of coil turns allows for suitable χ at larger distances. Larger coil diameter had a similar effect on χ with separation and misalignment, namely that with larger coil diameters larger misalignment and coil separations are possible. Increased frequency also

allows for greater separation and misalignment. Wire diameter had little effect on $\chi$, but pitch had a large effect. Tighter coil winding resulted in larger $\chi$ at greater distance. According to the results from this section, the best $R_x$ coil design consists of a one to three turns, is made from 1.1-1.3mm diameter wire, has a small pitch, and coil diameter between 12cm and 14cm.

## 5.3 Prototype Design

The prototype system design was selected based on simulation results, as well as results reported in [14]. The results from [14] indicate that coils with similar diameters achieve the best efficiency. A coil approximately the size of the selected MAV is appropriate as it conveniently attaches to the MAV. As mentioned previously, the best transfer efficiency occurs when $R_x$ and $T_x$ coils have similar diameters. Therefore, the $T_x$ coil size is selected also according to the MAV size. The simulation results are presented below and indicate acceptable coil geometries.

To determine $\chi$, it is necessary to characterize the power consumption vs. thrust relationship of an MAV. The MAV selected for this work is the Jianjian Technology Co., LTD model JJRC-H98 quadcopter drone. The control board from the MAV was removed and replaced with a Bitcraze Limited Crazyflie 2.0 quadrotor drone control board. The MAV was connected to a DC power supply and adhered to a scale. The initial mass of the MAV was recorded. The DC power supply was set to output between 3.8 and 4.0 volts. The MAV was started and the input thrust varied. At different levels of thrust the mass, current, and voltage were recorded. The mass measured while the MAV was operating was subtracted from the initial mass of the MAV to determine the amount of thrust at corresponding power. A plot of the gathered data is shown in Figure 5.11.

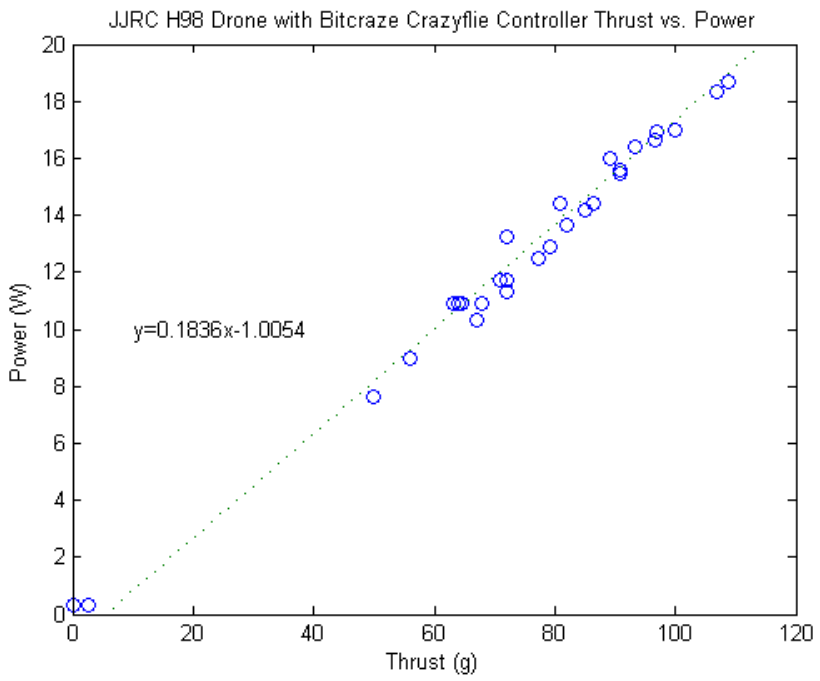


Figure 5.11: The relationship between thrust and power requirement of the MAV. The MAV is made of a JJRC H98 quadrotor frame, motors, and propellers, and a Bitcraze Crazyflie controller. The maximum power consumed by the MAV is 18.7W at a corresponding thrust of 108.8g. The equation of the linear fit for the data is shown in the plot.

A linear fit was used to determine an approximate equation to represent the relationship between thrust and power. The equation was found to be

$$Power(W) = 0.1836 \times Thrust(g) - 1.0054 \quad (5.1)$$

with an $R^2$ value of 0.9731. It was expected that the power-to-thrust relationship would be a polynomial fit, and both second order and third order polynomial fits were attempted on the data. A second order polynomial fit resulted in the relationship equation

$$Power(W) = -0.0002 \times (Thrust(g))^2 + 0.2116 \times Thrust(g) - 2.4136 \quad (5.2)$$

with an $R^2$ value of 0.9732, and a third order polynomial fit results in the relationship equation

$$Power(W) = -8 \times 10^{-6}\big(Thrust(g)\big)^3 + 0.0018\big(Thrust(g)\big)^2 + 0.0634(Thrust(g)) + 1.3136 \tag{5.3}$$

with an $R^2$ value of 0.9734. Due to the marginal increase in $R^2$ fit and the small polynomial coefficients, a linear fit to the data is considered acceptable.

The approximated equation for MAV power-thrust relationship is used with the model to calculate required power given a coil mass. In other words, the calculated mass is used as the required thrust. The MAV power requirement is determined using the established relationship.

Using the circuit model equations from Chapter 3 and the MAV power requirement model from above, $\chi$ can be calculated for many different coil geometries. Using simulated coil parameters for the $T_x$ coil shown in Figure 4.1, $R_x$ coil diameter, number of turns, pitch, and wire diameter are varied and surface plots are generated to understand the relationship between $\chi$ and varied coil parameters. For these simulations, the separation is held constant at 100mm between the $R_x$ and $T_x$ coils, but any separation can be used. The simulations are performed using two different RF power sources. The first simulated power source is a power source with no limit on current, but has a 50V input. The second simulated power source has a voltage limit of 50V, a current limit of 2A, and a power limit of 100W. These values represent limitations of the RF power amplifier used in this work. The plots summarizing the results of the simulations are

included in the following figures.

The RF power supply used in this work has a limited output of approximately $50V_{RMS}$ and $2A_{RMS}$. With limited power input, there is a general ridge indicating that with an Rx coil diameter of 200mm, the ideal number of turns is one or two. At smaller diameters (8-9cm), the ideal number of turns increases to four or five.

Figures 5.12 and 5.13 demonstrate how $\chi$ changes with varying $R_x$ coil diameter and number of turns. The jagged peaks seen in Figure 5.13 are a result of changing voltage and current inputs. With a maximum power input of 100W, 2A, and 50V, the simulation is programmed to maintain power at or below 100W. When a voltage or

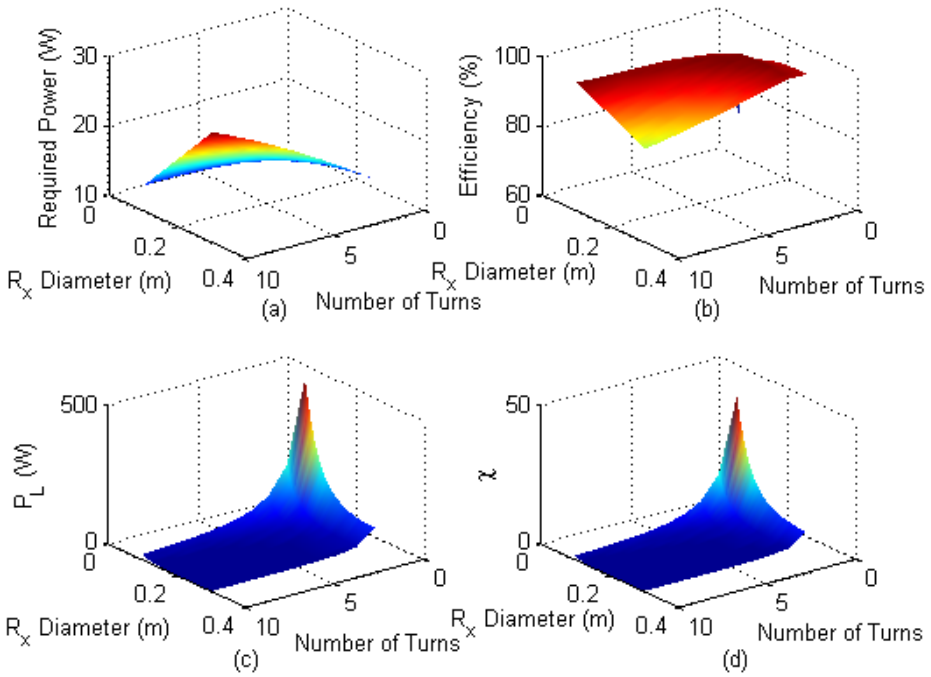


Figure 5.12: The effect on $\chi$ by the number of $R_x$ coil turns and outer diameter: (a) power required to lift the MAV, (b) efficiency of the WPT system, (c) $P_L$, and (d) $\chi$, according to the modeled equations. In this simulation, a voltage input from the power supply is 50V but no current limitations were put in place, hence the high power received at the load. The simulated pitch is 2mm.

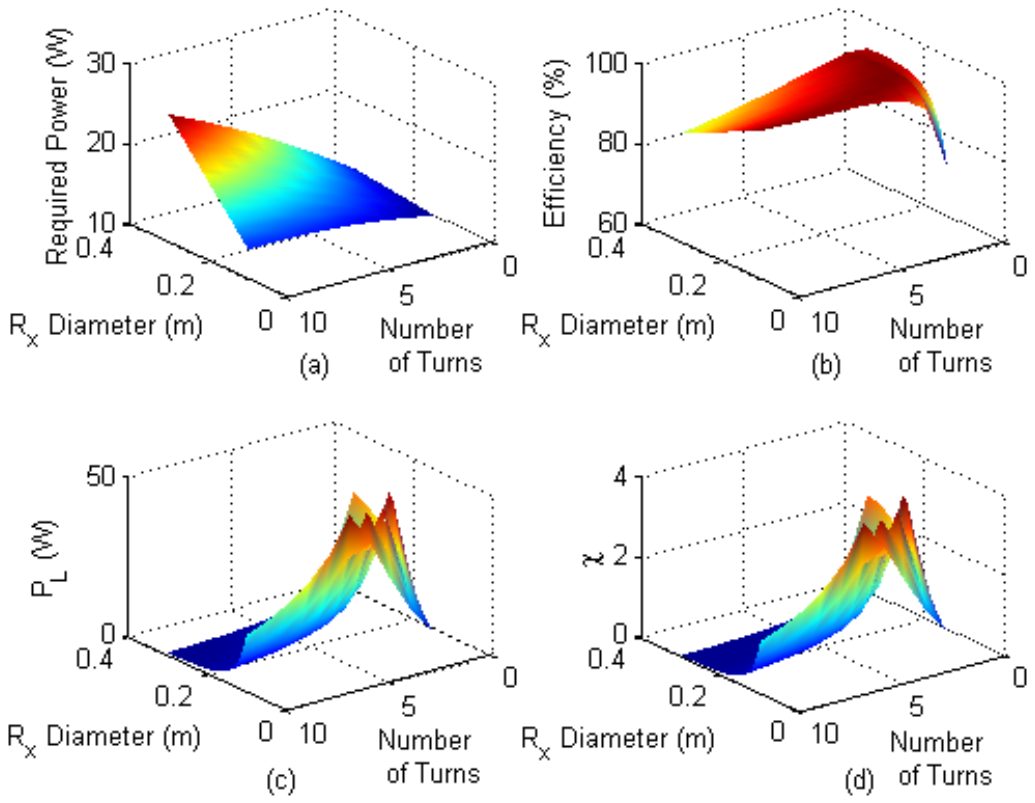


Figure 5.13: Performance of the WPT system when power input is limited by a maximum $V_{in}$ of 50V and maximum $I_1$ of 2A, which is approximately the limitations of the RF Power supply used in this work. The jagged peaks are a result of a changing power depending on different combinations of voltage and current to achieve 100W. Parameters varied are $R_x$ diameter and number of $R_x$ coil turns. The plots are (a) power required to lift the MAV, (b) efficiency of the WPT system, (c) $P_L$ and (d) $\chi$. The simulated pitch is 2mm.

current exceeds their respective limit, the program resets the offending power variable to the limit and calculates the other based upon the reset variable. This results in some jumps in power output, which are seen in the jagged peaks.

The comparison of $R_x$ coil pitch and number of turns to $\chi$ and other RIPT system performance values without current limitations, as shown in Figure 5.14, indicate that the best combination of pitch and number of turns to achieve the highest $\chi$ is a pitch of 3-4cm

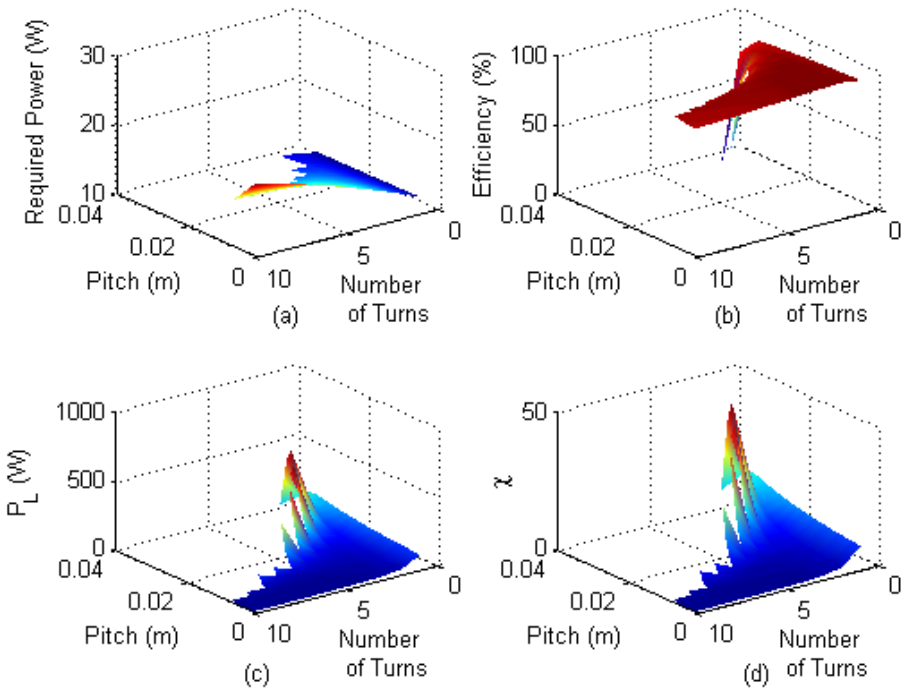


Figure 5.14: The effect on $\chi$ by the number of $R_x$ coil turns and pitch: (a) power required to lift the MAV, (b) efficiency of the WPT system, (c) $P_L$ and (d) $\chi$, according to the modeled equations. A voltage input of 50V was set, but no current limitation was set. This plot indicates that as number of turns decrease the pitch of the coil should decrease to maintain high $\chi$.

and one turn. A one-turn spiral with such a large pitch would make the slope of the spiral very aggressive as it spins inward, but does not overlap.

The plots investigating the relationship between $\chi$, coil turns, and pitch shown in Figure 5.14 and Figure 5.15 indicate that there are several combinations of turns and pitch size, which would result in acceptable results. The results in Figure 5.15 are more useful in practical applications since the power supply in this work is not without limits.

Those results show a ridge that appears to have a high points at approximately two turns and 1cm pitch. Several other combinations would be suitable, however, including a coil with nine to ten turns and 2cm pitch. Because the desired output of the

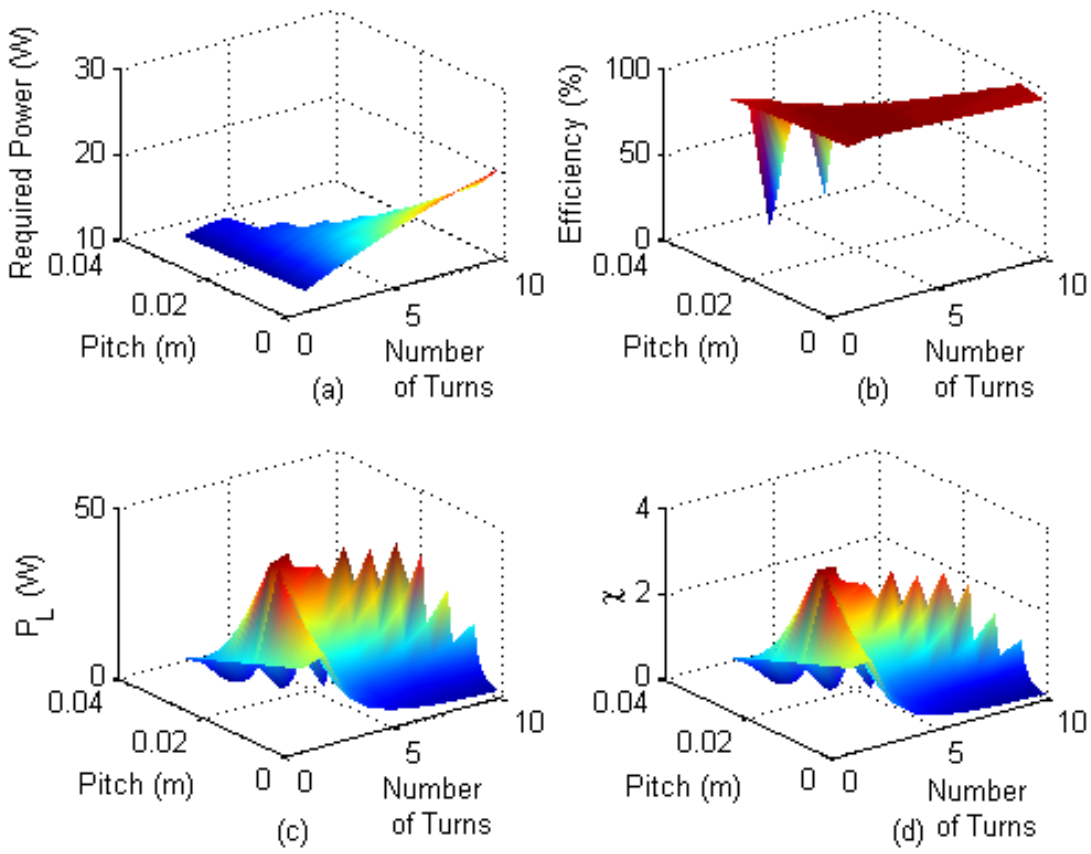


Figure 5.15: An example of the effect on $\chi$ by the number of $R_x$ coil turns and pitch: (a) power required to lift the MAV, (b) efficiency of the WPT system, (c) $P_L$, and (d) $\chi$, according to the modeled equations. Input power was limited in this simulation to 100W with 50V and 2A upper limits. The results here indicate that for high $\chi$ a small number of turns (one to two) should be used with a small pitch.

simulations is to determine the maximum possible value of $\chi$, the two turn and smaller pitch size option is desirable.

The results of simulation comparing $R_x$ wire diameter, coil turns, and $\chi$ without an input current limit suggest that the best combination of wire diameter and number of turns is one turn and diameter of approximately 0.8mm. As with previously discussed plots, because the simulation that generated these results did not have a current limitation, the plots in Figure 5.16 are not as useful as those in Figure 5.17 because the results in

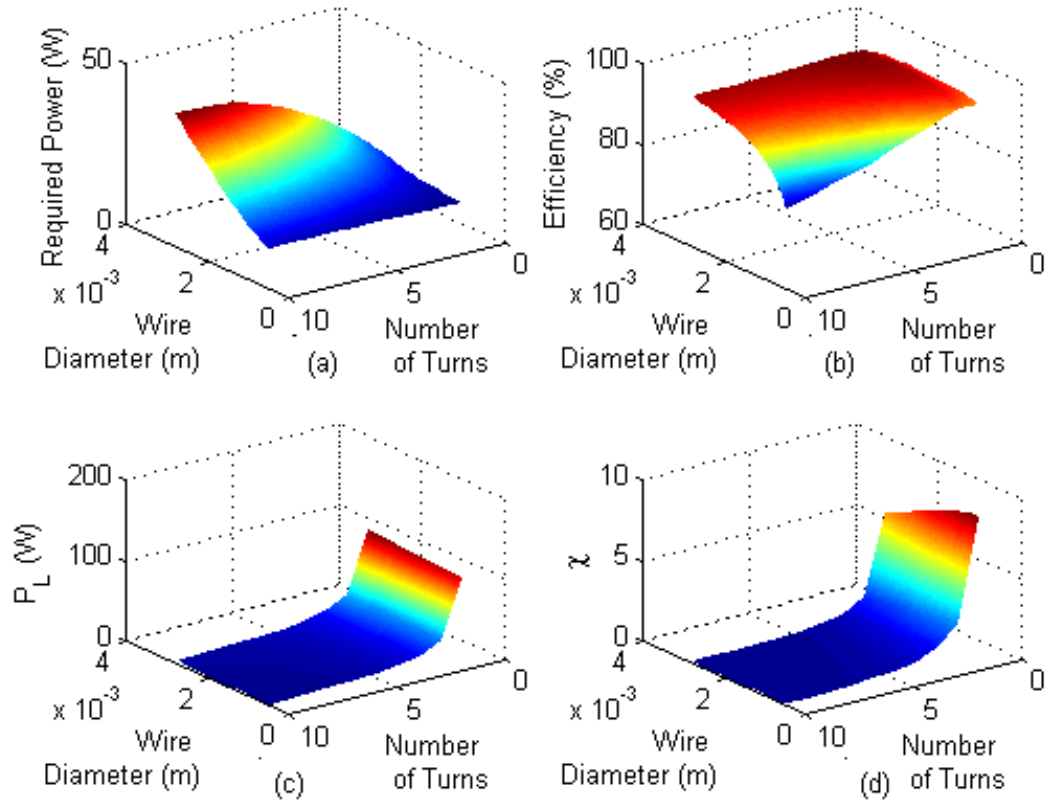


Figure 5.16: The effect on χ by the number of $R_x$ coil turns and wire diameter: (a) power required to lift the MAV, (b) efficiency of the WPT system, (c) $P_L$ and (d) χ, according to the modeled equations. Without a current limitation the results indicate that few coil turns and small wire diameter are the best way to achieve high χ.

Figure 5.17 are more realistic to a real power supply. In the case of comparing number of turns to wire diameter, both uncapped current results and limited power input results indicate that using a smaller wire diameter with fewer turns increases χ the most. Therefore, the chosen coil geometry will be made up of one to two turns and wire of diameter less than 2mm. Based on the analysis from the preceding figures, a suitable coil geometry was determined that would achieve χ greater than 1 and provide an MAV with enough power to hover. The coil parameters are summarized in Table 5.2.

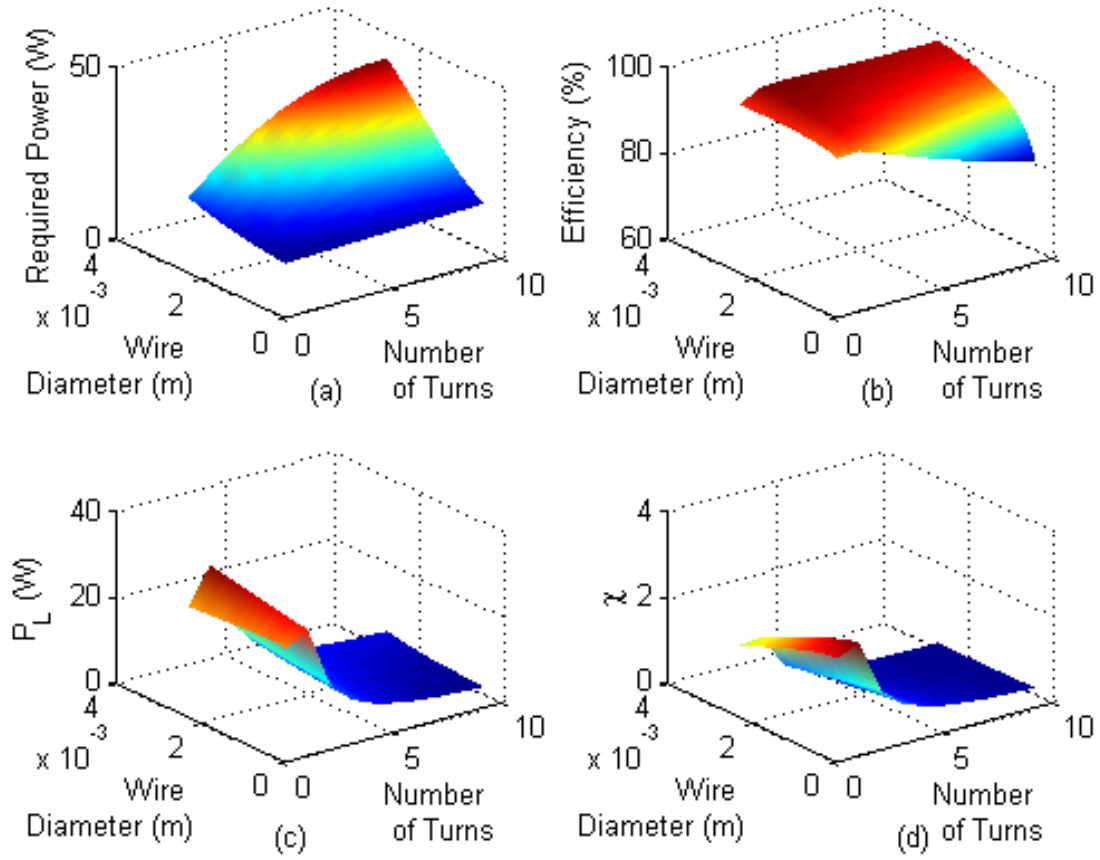


Figure 5.17: The power input is limited to 100W, 50V, and 2A in this simulation. The effect on $\chi$ by the number of $R_x$ coil turns and outer diameter: (a) power required to lift the MAV, (b) efficiency of the WPT system, (c) $P_L$, and (d) $\chi$, according to the modeled equations are shown. With a power limitation set in place this plot indicates that a ridge occurs, and to maximize $\chi$ few turns should be used with small wire diameter (0.8-1.3mm).

Table 5.2: Summary of suitable $R_x$ coil parameters to provide an MAV with enough power to hover, achieving $\chi$ greater than 1.

| | **Determined $R_x$ Coil Parameters** |
|---|---|
| **$R_x$ Number of turns** | 2 |
| **$R_x$ pitch (mm)** | 1 |
| **$R_x$ outer diameter (cm)** | 14 |
| **Frequency (MHz)** | 13.56 |
| **$R_x$ wire diameter (mm)** | 1.3 |

### 5.3.1 Electronic Components

In order to power an MAV, the power must be conditioned from high frequency alternating current to direct current. The input voltage to the MAV controller must be between 3.7V and 4.0V in order for the controller to operate correctly. To convert from AC to DC in the Megahertz range can be difficult due to component limitations. Several methods exist to convert the received power to DC including half-wave or full-wave bridge, Class E, Class D, Class F, Class $EF_2$ rectifiers [27], and harmonically terminated rectifiers [35]. According to Ganti *et al.* in [35], the most suitable rectifying circuit for a high power, high frequency application is one which terminates second and third order harmonics of the desired operating frequency, as shown in Figure 5.18. The principle behind the operation is that odd harmonic components of the input signal are open circuited, while all even harmonic components are short circuited. By doing this, the circuit can be tuned to shape voltage and current such that there exists zero voltage switching across the diode, which can result in high efficiency rectification.

The harmonically terminated rectifier has a reported maximum efficiency of 84%, which is less efficient than some methods involving controlled switching electronics. However, due to the simplicity of the circuit and the lack of extra electronic controllers needed, the harmonically terminated rectifier is suitable for this work.

To regulate the voltage from the rectifier, a DC-DC buck-boost converter was selected. A DC-DC converter in the WPT system can provide some degree of impedance matching [31]. Due to the low impedance of the MAV while hovering, the voltage drop across the MAV can be quite low. The DC-DC converter can help boost the voltage if it drops too low. It was determined that a minimum voltage input of 3.0V to a DC-DC is suitable for this work. The LDO10C-005W05-HJ DC-DC converter made by Artesyn

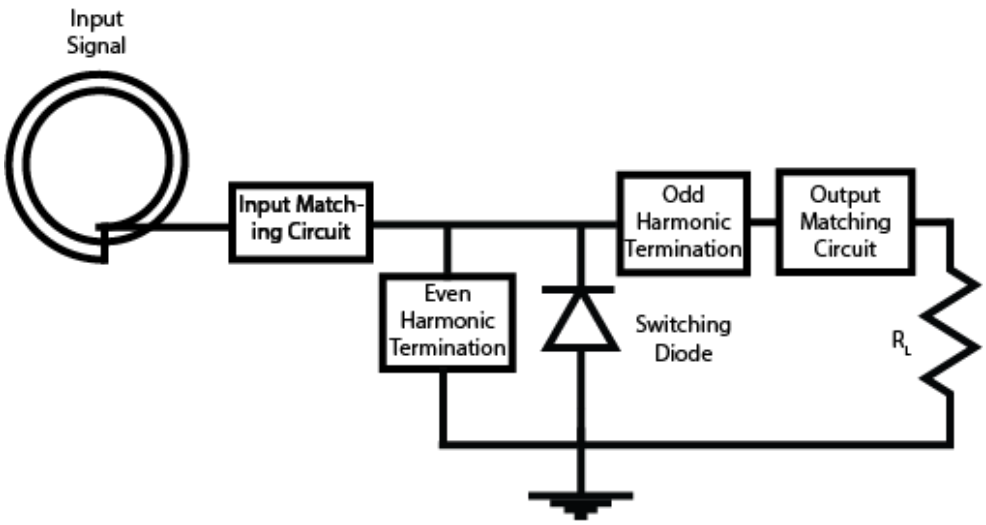


Figure 5.18: A simplified circuit model of the harmonic rectifier, adapted from [35], is shown here. The even harmonic termination circuit is a series LC circuit, which resonates at approximately twice the operating frequency. The odd harmonic termination is a parallel LC circuit, which resonates at approximately three times the desired frequency.

Embedded Technologies was selected. The maximum input voltage to the selected DC-DC is 13.6V, which is exceeded when the MAV is starting up. Therefore, to prevent damage to the DC-DC and MAV controller, 13V Zener diodes are placed in parallel to the MAV input. The final power conditioning circuit is shown in Figure 5.19.

In this chapter, a sensitivity study was performed to determine which design parameters have the largest effect on $\chi$. It was determined that coil pitch, number of turns, and coil diameter have a significant impact on the performance of the RIPT system. Wire diameter did not have a large impact, materials considered all performed similarly, and frequency was fixed based on federal regulations. With the presented model from Chapter 3, and by characterizing an off-the-shelf MAV, the figure of merit $\chi$ was explained and many combinations of coil design parameters were simulated, including $R_x$ number of turns, wire diameter, pitch, and coil diameter. Analysis of the simulation

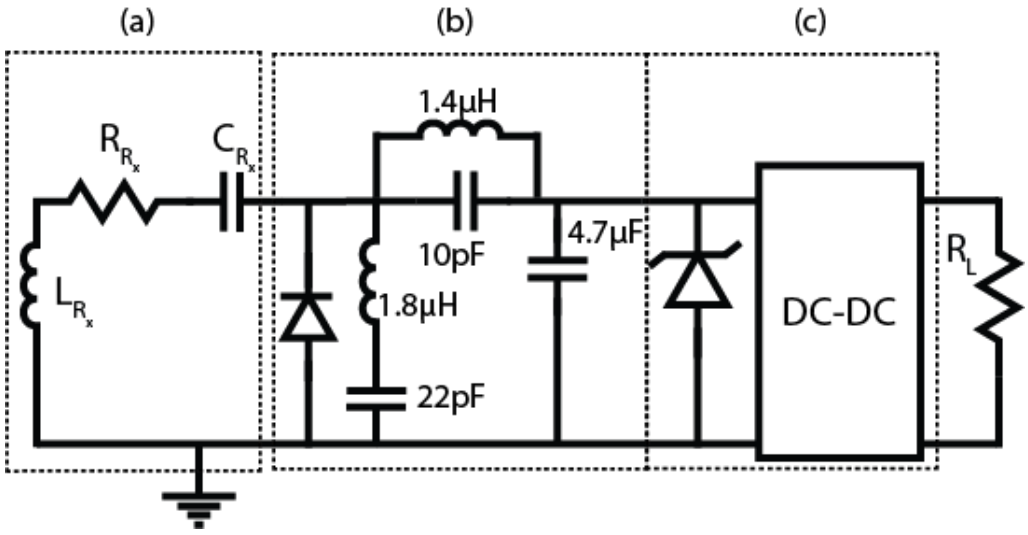


Figure 5.19: The circuit model for the $R_x$ coil and power conditioning electronics is shown here. The circuit is divided into sections: (a) the $R_x$ coil, which provides the input to the rest of the circuit, (b) the harmonically terminated rectifier used to convert AC power to DC, and (c) the voltage regulation, which precedes the MAV load $R_L$.

results pointed toward a suitable coil geometry to achieve acceptable $\chi$.

Based on the results presented in this chapter, an acceptable $R_x$ coil geometry is determined. A 137 mm outer diameter coil made of two turns of 16 AWG wire (1.29mm diameter) and close pitch (1mm) is found to provide enough power to the MAV while maintaining low coil mass. Such a coil was used in Chapter 4 and shown in Figure 4.2(a).

# CHAPTER 6

# FULL MAV SYSTEM VALIDATION

Based on the results obtained in Chapter 5, a power conditioning circuit was constructed and attached to the selected $R_x$ coil, and the output attached to the MAV input. In this chapter, the designed WPT system is assembled and tested to validate that sufficient power can be supplied to an MAV using the WPT system. Experimental procedures are discussed, as well as test results.

## 6.1 Experimental Setup and Procedure

To test the WPT design with the selected MAV, the designed coil was built and attached to the MAV. String was used to tie the coil to the frame of the MAV. The coil was connected to the rectifying and power regulation circuit, and the output of the circuit was connected to the motors of the MAV. In this experiment, the MAV was not powered through the controller. A platform was constructed approximately 90mm above the $T_x$ coil and the MAV was placed on the platform. Two thin rods were fixed to the platform and placed through the front and back of the MAV frame to limit motion to the vertical axis. The $T_x$ coil was attached to an MFJ 939 L-network automatic tuner. The tuner was used if reflected power from the WPT system exceeded 30W, but otherwise remained offline. Another MFJ 945E tuner was also connected in series, but remained offline. The MFJ 945E tuner contains a power/SWR meter, which was used to monitor forward and

reflected power in the system. The WiBotic, Inc. RF power amplifier was then connected.

To begin the experiment, the RF power amplifier was powered on, beginning at low power. An oscilloscope probe was connected to the output of the DC-DC converter to monitor output voltage. It was confirmed that the output of the DC-DC converter is between 3.7 and 4.0 volts. It was also noted that by connecting the probe, the WPT system became detuned. The probe also adds extra weight, which exceeds the MAV's ability to carry in this setup. Therefore, it is not possible to actively measure power delivered to the MAV while hovering. The power from the power supply was slowly increased until the MAV began to hover. The power was then turned up to the maximum output. A picture of the test setup is included in Figure 6.1.

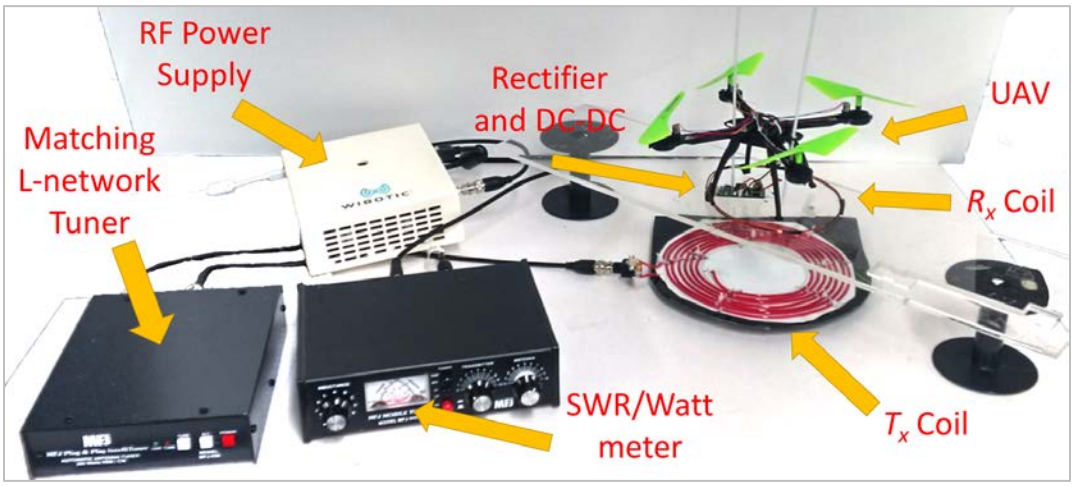


Figure 6.1: The WPT system with the MAV is shown here. The MAV is positioned on a platform approximately 90mm above the $T_x$ coil. The MAV motors are connected directly to the output of the DC-DC converter, which is connected to the rectifying circuit. The $R_x$ coil is tied to the MAV. The $T_x$ coil is connected to a power/SWR meter, a tuning L-network, and then connected to the RF power supply. The posts from the platform guide the MAV vertically directly above the $T_x$ coil.

## 6.2 Experimental Results

Using the methods described above, sufficient power was transferred to an MAV in order to allow it to hover, which is shown in still frames in Figure 6.2. Because active measurement of power delivered to the MAV is not possible, the power delivered to the MAV is estimated using the data to characterize the MAV power vs. thrust. The $R_x$ coil, DC-DC converter, and rectifying circuit have a combined mass of 23 g. The MAV has a mass of 46 g, thus the total mass of the MAV with coil and power conditioning electronics attached is 69 g. According to the characterized model, the MAV requires approximately 11.7 W to hover in place. The recorded input power from the RF power supply was 37 W. The theoretical $\chi$ for the given test setup is approximately 2. The model calculates $P_L$ at the point in the circuit between the $R_x$ coil and the power conditioning electronics. The power conditioning electronics have an estimated overall efficiency of DC regulator. The resulting experimental $\chi$ including power conditioning losses is between 1.4 and 1.67 at a separation of 114mm above the $T_x$ coil. At the simulated

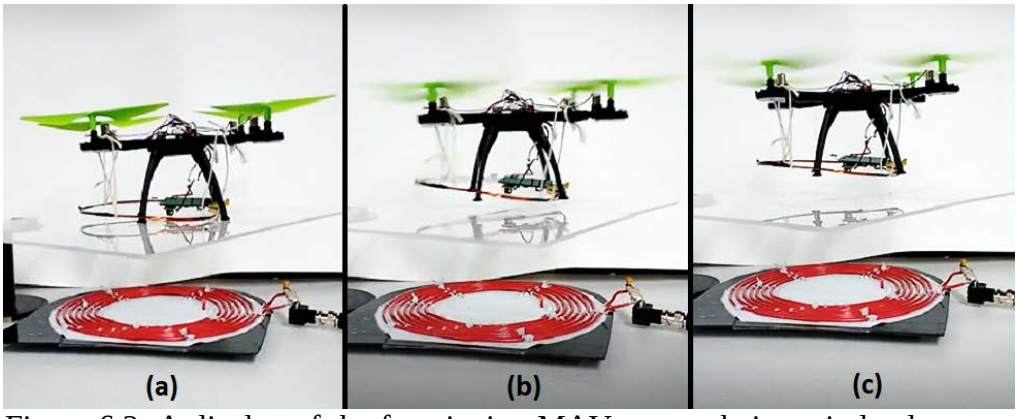


Figure 6.2: A display of the functioning MAV system being wirelessly powered. The MAV hovers 114 mm above the $T_x$ coil and is guided by thin guidewires to remain above the $T_x$ coil. The MAV with $R_x$ coil and power electronics has a mass of 69 g and requires approximately 12 W to hover as shown.

60% to 75%, according to published data for the rectifier and datasheet data for the DC-100mm above the $T_x$ coil, the coupling is closer to the critical coupling value and would therefore result in a higher $\chi$.

The area above the $T_x$ coil in which the MAV can receive sufficient power and remain hovering is approximately a 4 cm radius about the axis of alignment with the $T_x$ coil. This was determined by moving the platform away from axial alignment and noting distance away from alignment and MAV performance. This radius is consistent with the experimental data gathered in Chapter 4. The vertical separation between the coils is more sensitive as the change in coupling is more dramatic with variation in separation than variation in misalignment. This is also consistent with previous findings when comparing the shape of peaks between Figure 5.1 and Figure 5.2.

The WPT system powering the MAV has been experimentally operated for several minutes before the power supply was turned off, but the system would be able to operate until component failure. It was noted that after approximately a half hour of experimentation with the WPT-MAV system being powered up and powered down once every 1-2 minutes, the brushed DC motors on the MAV began to heat up considerably and affected the performance of the MAV.

# CHAPTER 7

# FUTURE WORK AND CONCLUSION

This work presents the successful modeling, analysis, and demonstration of a wirelessly powered quadcopter drone by analyzing how the defined figure of merit, $\chi$, changes with changing RIPT system parameters. There are several ways in which this work can be improved, which will be discussed in this chapter.

## 7.1 Future Work

In future work, the power conditioning electronics can be included in the model of the RIPT system to better predict system performance. This would enable a better prediction of $\chi$ and indicate if impedance matching methods are necessary. Efficiency in the power conditioning electronics was not measured. However, based on reported data for both the rectifier and the DC-DC voltage regulator, the overall efficiency of the power conditioning electronics is estimated to be between 60% and 75%. By designing a custom DC-DC voltage regulator, the efficiency of the power conditioning system could be increased and power delivered to the MAV improved. The weight of the components could be reduced by selecting different components or designing a custom DC-DC regulator. Custom power conditioning electronics could also be used to better handle changes in coupling as the position of the $R_x$ coil changes with respect to the $T_x$ coil.

A major way in which this work could be improved and expanded would be to

design and build a custom RF power supply. A custom Class EF inverter for a dynamic load was investigated in [36]. Inverters convert an incoming DC power supply into AC power, which oscillates at the desired frequency. Class E inverters are often used for frequencies in the multi-megahertz range but are not robust for changing loads. Class F inverters rely on harmonics of the designed circuit to achieve zero voltage switching. A combination of the two, a Class EF inverter, can achieve high efficiency over a wide range of loads, and can also be designed to have an output impedance, $Z_s$, closer to the 1Ω impedance of the MAV. By using a specialized power supply the power transfer could be improved, as well as efficiency. A custom designed power supply could also be more capable of providing consistent power as the $R_x$ coil moves with respect to the $T_x$ coil. Another advantage of a custom power supply is that it would eliminate the need for impedance matching by tuning $Z_s$ to the needed impedance for the system.

In future work, it would also be beneficial to analyze how changing the $T_x$ coil geometry and size affects $\chi$. This would be an interesting angle of approach to the problem because the $T_x$ coil would not affect $P_{req}$, only $P_L$. Analyzing multiple different $T_x$ coil geometries would likely indicate that there exists a geometry that achieves a higher $\chi$.

## 7.2 Conclusions

This work discusses the design, modeling, analysis, and experimental demonstration of a resonant inductive power transfer system sufficient to power a small, 14cm MAV while hovering. A figure of merit, $\chi$, is the primary focus of this work, which compares the power delivered to the load of a RIPT system with the power required by an MAV to hover with the additional weight of the coil. The model presented in this work is

used to simulate many coil geometries as part of the RIPT system and select coil geometries, which result in $\chi$ greater than 1, enabling the MAV to hover. A suitable receive coil geometry was selected, and the selection was validated by demonstrating successfully wireless power transfer sufficient to power an MAV. A seven turn, 19cm diameter, 5mm pitch transmit coil paired with a 13.7cm diameter, two turn, 1mm pitch receive coil was built. An RF power supply with 50 Ω source impedance was used to deliver 37W to the RIPT system and to enable an MAV weighing 69g to hover 114mm above the transmit coil, consuming approximately 11.4W.

REFERENCES


[1] D. Loesche, “Drones: a tech growth market in the United States,” *Statista*, 2017. [Online]. Available: https://www.statista.com/chart/9525/sales-of-consumer-drones-to-dealers-in-the-us/. [Accessed: 10-May-2017].

[2] G. M. Plaizier, E. Andersen, B. Truong, S. Roundy, and K. K. Leang, “Design, modeling, and analysis of inductive resonant coupling wireless power transfer for micro aerial vehicles (MAVs),” in *IEEE Int. Conf. Robot. Autom.*, May 2018, (Submitted).

[3] M. C. Achtelik, J. Stumpf, D. Gurdan, K.-M. Doth, "Design of a flexible high performance quadcopter platform breaking the MAV endurance record with laser power beaming", *Proc. IEEE Int. Conf. Intell. Robots Syst.*, Sep. 2011, pp. 5166-5172.

[4] H. A. Foote, “Microwave-powered aircraft,” U.S. Patent 5 503 350, Apr. 2, 1996.

[5] N. Tesla, “System of signaling,” U.S. Patent 725 606, Apr. 14, 1903.

[6] A. Tomar and S. Gupta, “Wireless power transmission : applications and components,” *Int. J. Eng. Res. Technol.*, vol. 1, no. 5, Jul., pp. 1–8, 2012.

[7] J. J. Schlesak, A. Alden, T. Ohno, "A microwave powered high altitude platform", *IEEE MTT-S Int. Microw. Symp. Dig.*, vol. 1, no. 2527, May, pp. 283-286, 1988.

[8] A. Kurs, A. Karalis, R. Moffatt, J. D. Joannopoulos, P. Fisher, M. Soljacic, "Wireless power transfer via strongly coupled magnetic resonances", *Science*, vol. 317, no. 5834, Jul., pp. 83-86, 2007.

[9] R. Whittle, “How it works: laser beaming recharges UAV in flight,” *Popular Mechanics*, 2012. [Online]. Available: http://www.popularmechanics.com/flight/drones/a7966/how-it-works-laser-beaming-recharges-uav-in-flight-11091133/. [Accessed: 01-Jan-2017].

[10] S. Valtchev, E.N. Baikova, L.R. Jorge, "Electromagnetic field as the wireless transporter of energy" in *Electronics and Energetics, Nis, Serbia:Facta Universitatis*, vol. 25, no. 3, Dec., pp. 171-181, 2012.

[11] D.-W. W. Seo, J.-H. H. Lee, and H. S. Lee, “Study on two-coil and four-coil

wireless power transfer systems using Z-parameter approach," *ETRI J.*, vol. 38, no. 3, Jun., pp. 568–578, 2016.

[12] D. S. Ricketts, M. J. Chabalko, and A. Hillenius, "Erratum: experimental demonstration of the equivalence of inductive and strongly coupled magnetic resonance wireless power transfer," *Appl. Phys. Lett.*, vol. 102, Apr., pp. 107, 2013.

[13] J. M. Arteaga, S. Aldhaher, G. Kkelis, D. C. Yates, and P. D. Mitcheson, "Design of a 13.56 MHz IPT system optimised for dynamic wireless charging environments," in *2016 IEEE 2nd Ann. So. Pow. Elec. Conf., SPEC 2016,* Dec. 2016, pp. 1–6.

[14] B. H. Waters, B. J. Mahoney, G. Lee, and J. R. Smith, "Optimal coil size ratios for wireless power transfer applications," in *Proc. IEEE Int. Symp. Circuits Syst.*, Jun. pp. 2045–2048, 2014.

[15] X. Shi *et al.*, "Effects of coil shapes on wireless power transfer via magnetic resonance coupling," *J. Electromagn. Waves Appl.*, vol. 28, no. 11, Apr., pp. 1316–1324, 2014.

[16] Solace Power, "Keeping UAVs in the Air with Wireless Power," *Solace Power*, Apr. 2016. [Online]. Available: https://static1.squarespace.com/static/5548d3d0e4b00b9ffc9a53e1/t/57191b804d088e0fae32af68/1461263233940/Keeping_UAVs_in_the_Air_Longer_with_Solace_Wireless_Power_Apr_2016.pdf. [Accessed Jan. 1, 2018].

[17] M. Koizumi, K. Komurasaki, Y. Mizuno, and Y. Arakawa, "Wireless power feeding with strongly coupled magnetic resonance for a flying object," *Wirel. Eng. Technol.*, vol. 3, no. 2, Jan., pp. 86–89, 2012.

[18] A. P. Sample, D. A. Meyer, and J. R. Smith, "Analysis, experimental results, and range adaptation of magnetically coupled resonators for wireless power transfer," *IEEE Trans. Ind. Electron.*, vol. 58, no. 2, Feb., pp. 544–554, 2011.

[19] S. Cheon, Y. H. Kim, S. Y. Kang, M. L. Lee, J. M. Lee, and T. Zyung, "Circuit-model-based analysis of a wireless energy-transfer system via coupled magnetic resonances," *IEEE Trans. Ind. Electron.*, vol. 58, no. 7, Jul., pp. 2906–2914, 2011.

[20] M. Kiani, U. M. Jow, and M. Ghovanloo, "Design and optimization of a 3 coil inductive link for efficient wireless power transmission," *IEEE Trans. Biomed. Circuits Syst.*, vol. 5, no. 6, Dec., pp. 579–591, 2011.

[21] J. Lee and S. Nam, "Fundamental aspects of near-field coupling small antennas for wireless power transfer," *IEEE Trans. Antennas Propag.*, vol. 58, no. 11, Aug., pp. 3442–3449, 2010.

[22] E. Bou, E. Alarcon, and J. Gutierrez, “A comparison of analytical models for resonant inductive coupling wireless power transfer,” *Prog. Electromagn. Res. Symp.*, no. 4, Aug., pp. 689–693, 2012.

[23] F. W. Grover, “The calculation of the mutual inductance of circular filaments in any desired positions,” *Proc. IRE*, vol. 32, no. 10, Oct., pp. 620–629, 1944.

[24] S. Babic, F. Sirois, C. Akyel, and C. Girardi, “Mutual inductance calculation between circular filaments arbitrarily positioned in space: alternative to grover’s formula,” *IEEE Trans. Magn.*, vol. 63, Sept., pp. 3591–3600, 2010.

[25] Office of the Federal Register, "Industrial, Scientific, and Medical Equipment: Operating Frequencies," *Electronic Code of Federal Regulations*, 47-I-A-18.301, 2017. [Online]. Available: https://www.ecfr.gov. [Accessed: Jan. 1, 2018].

[26] J. Dai and D. C. Ludois, “A survey of wireless power transfer and a critical comparison of inductive and capacitive coupling for small gap applications,” *IEEE Trans. Power Electron.*, vol. 30, no. 11, Nov., pp. 6017–6029, 2015.

[27] S. Aldhaher, D. C. Yates, and P. D. Mitcheson, “Design and development of a class $EF_2$ inverter and rectifier for multi-megahertz wireless power transfer systems,” *IEEE Trans. Power Electron.*, vol. 31, Mar., pp. 8138–8150, 2016.

[28] M. Li, P. S. Heljo, and D. Lupo, “Organic rectifying diode and circuit for wireless power harvesting at 13.56 MHz,” *IEEE Trans. Electron. Devices*, vol. 61, no. 6, Jun., pp. 2164–2169, 2014.

[29] K. Fotopoulou and B. W. Flynn, “Wireless power transfer in loosely coupled links: coil misalignment model,” *IEEE Trans. Magn.*, vol. 47, no. 2, Feb., pp. 416–430, 2011.

[30] M. Defilippo, “Highly resonant induction power transfer for underwater battery recharging,” MIT Sea Grant AUV Laboratory, Cambridge, Massachusetts, Tech. Report. 14-19, 16 Apr. 2015.

[31] Y. Huang, N. Shinohara, and T. Mitani, “Impedance matching in wireless power transfer,” *IEEE Trans. Microw. Theory Tech.*, vol. 65, no. 2, Feb., pp. 582–590, 2017.

[32] M. Fu, T. Zhang, X. Zhu, C. Ma, "A 13.56 MHz wireless power transfer system without impedance matching networks", *IEEE Wireless Power Transfer Conf.*, May 2013, pp. 222-225.

[33] R. Schmitt, “Radiation,” in *Electromagnetics Explained : A Handbook for Wireless/ RF, EMC, and High-Speed Electronics*, Elsevier Science. New York: Newnes, 2002, pp. 89–109.

[34] H. Zhou, B. Zhu, W. Hu, Z. Liu, and X. Gao, “Modelling and practical implementation of 2-coil wireless power transfer systems,” *J. Electr. Comput. Eng.*, vol. 2014, Sept., pp. 1–8, 2014.

[35] A. Ganti, J. Lin, R. A. Chinga, and S. Yoshida, “Harmonically terminated high-power rectifier for wireless power transfer,” *Wirel. Power Transf.*, vol. 3, no. 2, Apr., pp. 75–82, 2016.

[36] S. Aldhaher, P. D. Mitcheson, and D. C. Yates, “Load-independent Class EF inverters for inductive w S. Aldhaher, P. D. Mitcheson, D. C. Yates, "Load-independent class EF inverters for inductive wireless power transfer", *Proc. IEEE Wireless Power Transf. Conf. (WPTC)*, May 2016, pp. 1-4.